Effects of different wind directions on ventilation of the surrounding areas of two generic building configurations in Hong Kong

Kai Yip Lee [a], Cheuk Ming Mak [a]*

[a] *Department of Building Services Engineering, The Hong Kong Polytechnic University, Hung Hom, Kowloon, Hong Kong, China*

ralph.ky.lee@connect.polyu.hk, cheuk-ming.mak@polyu.edu.hk

*Corresponding author.

E-mail Address: cheuk-ming.mak@polyu.edu.hk (C.M.Mak).

Telephone: +852 2766 5856

Fax: +852 2765 7198

Abstract

This study investigated the effects of incident wind angles on wind velocity distributions in the wakes of two generic building configurations, namely, "T”- and "+"-shaped, and the air pressure distributions along their leeward walls by using computational fluid dynamics simulations. Results show that when the wind approaches laterally (90°) (versus when the wind is direct (0°)), the downwind length and maximum bilateral width of the low-wind velocity zone in the wake of “T”-shaped building decrease by 11.5% and 37.9%, respectively. When the incident wind is oblique (45°) (versus when it is direct), the length and width of this low-wind velocity zone in the wake of “+”-shaped building decrease by 15.0% and 30.9%, respectively. Furthermore, results show that the air pressure on the leeward walls of the “T”- and “+”-shaped buildings gradually decreases along with the building height. The resulting low-wind conditions on the upper floors of the buildings reduce the fresh air intake of their leeward units utilizing natural ventilation. It is particularly apparent in the case of direct approaching wind. Thus, the appropriate selection of building configurations and their orientations allows for the most effective use of wind to enhance ventilation in indoor and urban environments.

Keywords: Airflow simulation; Leeward wall air pressure distribution; Building

configurations; Building wake effect; Incident wind angles.

Introduction

Outdoor environmental factors like wind velocity and airflow sufficiency play an essential role in enhancing thermal comfort for human beings, diluting air pollutants in urban areas, and improving the air quality in the urban locality. [1-4] Low wind speeds promote the accumulation of air contaminants inside street canyons that adversely affect the air quality in an outdoor environment. [5, 6] However, too strong wind around a building may cause discomfort or even danger to pedestrians. [7] Thus, to strike a balance is crucial by achieving an acceptable level of wind comfort and allowing an urban area to self-ventilate, but it is rather tricky and challenging. [8] The problem is particularly significant in a subtropical metropolitan area such as Hong Kong. Hence, the Hong Kong SAR Government proposed the air ventilation assessment (AVA) scheme to improve the air movement at the pedestrian level in Hong Kong by devising effective measures to maximize the benefits of wind and enhance ventilation and breathability within the urban environment. [9]

However, the benefit of sufficient airflow in the outdoor environment could be significantly diminished and offset by the blockage effects from buildings or other urban structures in an urban setting. [6, 10-12] The effects of the reduced wind speeds are particularly apparent in the building wakes and leeward sides of the buildings. Building shapes and orientations influence the environmental wind conditions, and their proper

design can help improve both the perceived wind comfort at pedestrian level [13] and the surface pressure distribution.[14] Because urban building layouts influence the wind distribution in an urban environment, numerous studies have proposed additional evaluation parameters, including the air change rate, age of the air, and ventilation efficiency, to assess the ability of a building to enhance a city's ventilation. [15-17] These parameters can be addressed by careful town planning and sufficient appraisal of the geometry of an urban setting. [18, 19]

Sufficient ventilation could enhance the thermal comfort of people engaged in outdoor activities in an urban environment. [7, 19-21] Research showed that a mean wind speed of 1.5 m/s for 50% of the time provides the most comfortable environment during the summer months in Hong Kong for pedestrians walking in the shade without additional thermal stress from solar radiation. [22, 23] This means areas with mean wind speeds lower than 1.5 m/s at the pedestrian level are considered low-wind velocity zones that are uncomfortable and unfavourable for pedestrian activities. [7]

Apart from thermal comfort, the blockage effect of buildings in an urban area could affect the wind velocity and the sufficiency of ventilation and subsequently impact the distribution of air contaminant in an urban setting. The distribution of air contaminants depends on the complex relationships between the atmospheric flow and flow around physical obstacles. [11] The wind flow patterns are also greatly affected by the incident

wind directions. [24] Several studies also found that the higher the wind speed, the lower the concentrations of pollutants due to better pollutant dispersion. [25-27]

Airflow velocity could influence not only the outdoor but also the indoor ventilation. The atmospheric airflow can enhance and control the pressure distributions on building surfaces in a naturally ventilated building, as the inward and outward flows of air are driven by the pressure differences produced by the wind or buoyancy effects. [28-30] Wind generates pressure differences among openings and promotes a robust airflow through an internal space. [28] Hence, it could also help dilute air contaminant and improve indoor air quality. [31, 32] However, wind force asserted on the building could distort the distribution of pressure profile of the building and affect the pattern of indoor airflow.[33] As such, the effectiveness of natural ventilation is sensitive to changes in window positions and building orientations,[34, 35] and choosing the right window positions and building orientation would positively impact the level of indoor natural ventilation. [31, 35, 36] Therefore, it is vital to study the relationships among the different shapes of obstacles or buildings and the incident wind angles to identify their effects on the distributions of wind velocities in the wakes and air pressure on the leeward surfaces of buildings.

Excellent studies of the wind flow around a cubical building have been performed. [7, 37-43] However, the impacts of this flow on the natural ventilation and thermal comfort

on the ground level of these buildings have not been adequately investigated. In particular, little research has been performed on wind effects from different directions on the flow in the wakes of buildings with configurations commonly found in Hong Kong. Hence, this study aims to examine the effects of wind from different directions on the wind velocity distributions in the wakes and the pressure distributions on the leeward walls of two buildings with configurations commonly found in Hong Kong by using computational fluid dynamics (CFD) simulations. It is hoping to shed some light on the principle of designing window positions and orientation of the generic buildings utilizing natural ventilation. Two residential building designs/configurations, the "T" shape (Figure 1a) and the "+" shape (Figure 1b), are found to be very common in the urban areas of Hong Kong. In this study, the comparisons of the wind velocities at the pedestrian level in the wakes of these two building shapes (under different wind directions) with the normal building configuration, "-" shaped building model, and the distribution of air pressures on their leeward walls were conducted. The turbulence model and computational settings were validated using wind flow data from the wind tunnel test results from the "Compilation of Experimental Data for Validation Purposes" (CEDVAL) project developed by the Meteorological Institute at the University of Hamburg. [44] The validated model and numerical settings were then used to simulate the two building shapes, together with the normal building configuration ("-"), under

different wind directions. As the wind flow pattern is closely related to the incident wind direction, three typical wind directions - the direct opposing ($\theta = 0°$ and $\theta = 180°$), oblique ($\theta = 45°$ and $\theta = 135°$), and lateral approaching wind directions ($\theta = 90°$) were selected and simulated using the CFD models. The wind flow patterns and wind velocity distributions in two locations - (i) near the leeward wall; and (ii) the building wakes (pedestrian level) of the two building configurations will be discussed in this paper.

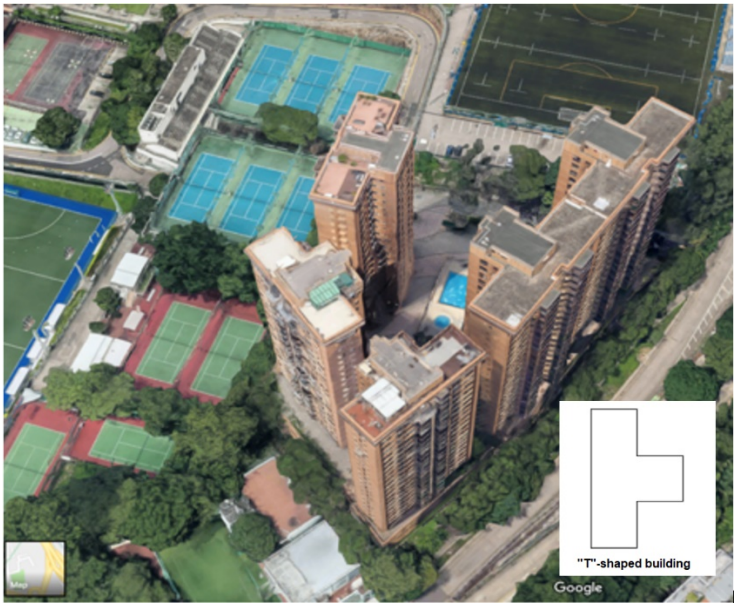

Figure 1(a). "T"-shaped building commonly found in Hong Kong (Source: Google Map)

Figure 1(b). "+"-shaped building commonly found in Hong Kong (Source: Google Map)

Methodology

CFD turbulence models

On-site measurement of air quality is a straightforward method for identifying the concentration and dispersion patterns of air pollutants in a defined environment. However, to perform such monitoring for an extended period is expensive and not always feasible.[2] Numerical CFD methods, which provide complete field data with no limitations on the similarity requirements, offer an alternative way to study the dispersion of air pollutants around a building.[4] Research showed that CFD could predict the air velocities around single, double, and multiple building configurations in a detailed quantitative fashion.[45] Experimental data, such as that from certain wind tunnel studies of the pollutant dispersion, can be used to validate the simulated results.

Xia, Niu et al. [46] and Blocken [47] stated that Reynolds-Averaged Navier-Stokes (RANS) approaches, which are commonly used for solving turbulence problems, are less computationally expensive than other transient state methods because they focus on the mean flow properties of turbulence. Among different RANS approaches, the realizable (RLZ) *k*-ε and renormalization group (RNG) *k*-ε models are suitable for simulating urban wind flow. [2, 48] An et al.[45] found that the RLZ *k*-ε model does well in predicting wind velocities in high-wind regions, but it tends to underestimate the flow in the low-wind areas. The RNG *k*-ε model, however, consistently provides more accurate results when compared with wind tunnel flow and pollutant concentration field data. [49-51] It provides satisfactory results when it is used to study wind-driven single-sided natural ventilation, [52] and it exhibits better performance for solving rapid strain and streamline curvatures. Its adaptiveness is achieved through the inclusion of an additional strain-dependent term (R_ε), [24] as shown in Equation (1):

$$R_\varepsilon = \frac{C_\mu \rho \eta^3 (1 - \frac{\eta}{\eta_0})}{1 + \beta \eta^3} \cdot \frac{\varepsilon^2}{k} \quad (1)$$

Here, C_μ, η_0, and β are constants (C_μ = 0.09, η_0 = 4.38, β = 0.012), ρ is the fluid density, *k* is the turbulent kinetic energy, ε is the turbulent viscous dissipation rate, and $\eta \equiv Sk/\varepsilon$ where *S* is the strain rate scale. According to ANSYS[53] code, the revised

feature in the RNG *k*-ε model allows it to effectively predict flows with low Reynolds (*Re*) numbers in near-wall regions. In view of their availability, consistency, and suitability, both RLZ and RNG *k*-ε models were selected in the validation process with CEDVAL wind tunnel data.

Description of wind tunnel

The wind tunnel tests from the CEDVAL project, developed by the Meteorological Institute at the University of Hamburg Environmental Wind Tunnel Laboratory, [44] were employed to validate our models (Figure 2). In our study, models in a 1:200 scale (with the actual measurement of each side, H, of the cube equivalent to 0.125 m) were constructed for direct comparison with the CEDVAL wind tunnel project. The test parameters are listed in Table 1. The similarity requirements between the wind tunnel and CFD models were strictly tested. The *Re* number was greater than 3.7×10^4, which achieves the minimum requirement of 1.5×10^4. [42] Hence, *Re* number independence was attained, and the similarity requirements were fulfilled.

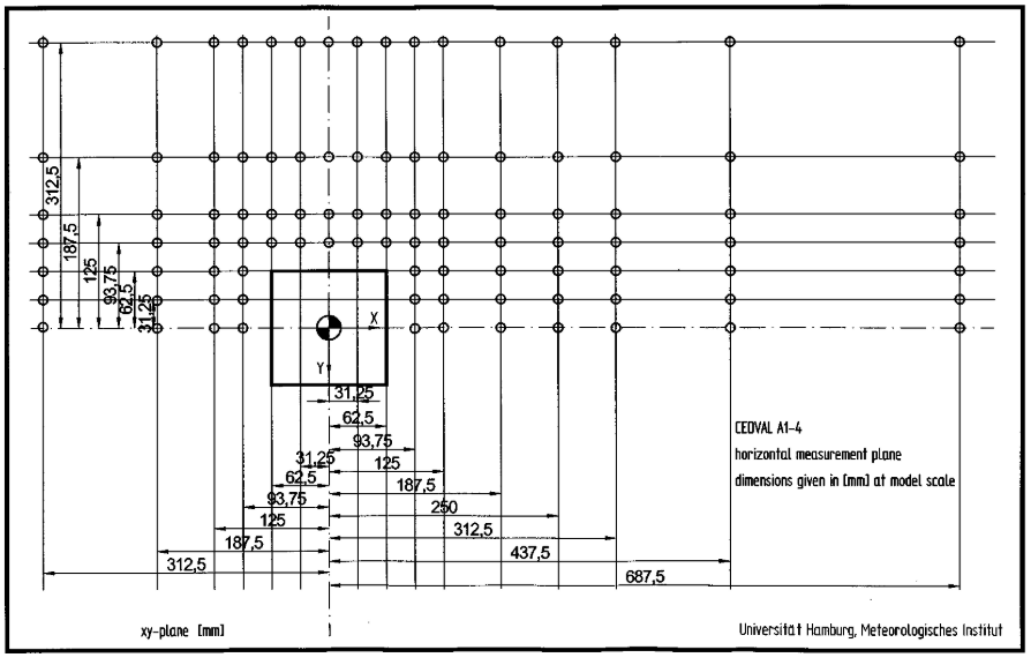

Figure 2. The setup sketch of the wind tunnel showing the measurement locations[44]

Table 1. Parameters for the scaled model (A1-4)[44]

Parameter	**Symbol**	**Value**
Building height	H	0.125 m
Reynolds number	Re	37,250
Power law	$\acute{\alpha}$	0.22
Reference velocity	U_{ref}	6 m/s
Reference height	H_{ref}	0.5 m
Friction velocity	u^*	0.35 m/s
Roughness height	z_0	0.0004 m
Offset height	d	0.00 m
Turbulence length	L	0.32 m

Boundary conditions

An inhomogeneous atmospheric boundary layer (ABL) and near-wall treatments can significantly affect the results of simulations of atmospheric flow and pollutant dispersion. [54] Hence, for an accurate simulation of the flow and dispersion of air pollutants, it was essential to develop a homogeneous ABL before conducting numerical studies.

Richards and Hoxey[55] suggested Equation (2) for the inlet boundary condition for a fully developed horizontally homogeneous two-dimensional ABL flow:

$$U = \frac{u^*}{K} ln\left(\frac{z + z_0}{z_0}\right) \quad (2)$$

To rectify the impracticality of the constant inlet profile for turbulence kinetic energy suggested by Richards and Hoxey, [55] and improve the consistency of horizontal boundary layer, turbulent kinetic energy (k) and turbulent viscous dissipation rate (ε) could be written as in Equations (3) and (4) to achieve the equilibrium between the turbulence dissipation and production: [44]

$$k = \sqrt{C_1\, ln(z + z_0) + C_2} \quad (3)$$

$$\varepsilon = \frac{u^* \sqrt{C_\mu}}{K(z + z_0)} \sqrt{C_1 ln(z + z_0) + C_2} \quad (4)$$

The inlet boundary conditions defined on the boundaries of the computational domain are determined by the profiles of the mean wind speed *U*, turbulent kinetic energy *k*, and turbulent dissipation rate *ε*, as indicated in Equations (2), (3), and (4), respectively. When incorporated into an appropriate near-wall treatment on the domain ground, this set of inlet boundary conditions allows one to obtain a homogeneous ABL. [54, 56] In Equations (3) and (4), *z* is 0.035 m (that is equal to 0.28 H in the model scale used in the determination of inlet boundary condition. [54, 57, 58]); z_0 is the roughness constant (0.0004 m); u^* is the frictional velocity (0.35 ms^{-1}); C_1 and C_2 are constants which are equal to 0.025 and 0.41, respectively; C_μ is a constant equal to 0.09; *K* is the Von Karman constant, which is equal to 0.4187.[1]

The downstream vertical boundary was modelled as an outflow. The sky was treated as a mirror plane. An enhanced-wall function was adopted for the surfaces of the building block, where the computational domain was non-slip. The mesh near the building and ground surfaces was refined to replicate the physical characteristics of the flow. To accurately simulate the approaching ABL flow in the computational domain, horizontal homogeneity was required, i.e., the vertical flow profiles prescribed at the inlet needed to be preserved on the domain before reaching the buildings. [59]

The low-Reynolds-number regions below the first grids and the effects on the entire wall-bounded flow could be ignored, as the standard wall functions directly link the walls and near-wall logarithmic layer with a series of semi-empirical formulae. [54] In the present study, an enhanced wall treatment, which integrated the flow variables down to the walls, was adopted for near-wall modelling, as it could resolve the viscous sublayer and compute the wall shear stress from a local velocity gradient normal to the wall. Moreover, it provided a more accurate prediction of the velocity distributions in the recirculation zones near the windward edges and in the building wakes. [49]

Computational domain and grid

To ensure that the wind flow was fully developed with minimum blockage effect, the upstream, downstream, lateral, and height components of the computational domain were set as 5H, 15H, 5H, and 5H, respectively (Figure 3), based on the requirements of the CFD practice guidelines. [60] The blockage ratio was approximately 2.7% and in conformance with the European Cooperation in Science and Technology (COST) Action 732. [60] The entire domain was constructed using structured hexahedral grids with a grid expansion ratio of less than 1.2 in both the horizontal and vertical directions. [61] The pressure and momentum equations were coupled using the SIMPLE (Semi-Implicit Method for Pressure-Linked Equations) algorithm, and a second-order upwind scheme was used in the discretization. The scaled residuals in the simulation were all

set as 10^{-5}, and convergence was obtained at this level.

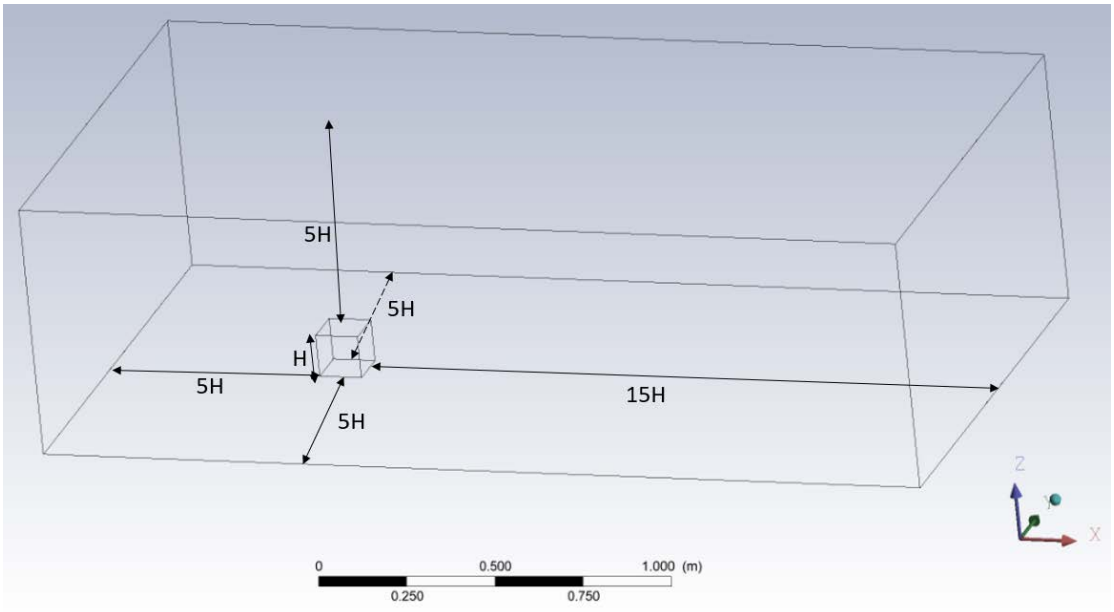

Figure 3. Computational domain

Grid-sensitivity analysis is important to reduce the discretization errors and computational time. [62] In this study, a grid-sensitivity analysis was performed based on three mesh systems. The three different mesh systems with minimum grid sizes of 0.0005 m, 0.0002 m and 0.00005 m, and mesh numbers of 1.443 million (coarse), 4.018 million (medium) and 6.079 million (fine), respectively, were constructed. The simulation results from the three systems were compared to examine the independence of the numerical solution in regard to the grid size.

Figure 4 shows the comparison of the dimensionless velocity ratio (U/U_{ref}) between the experimental wind tunnel data and the simulation results with RNG k-ε

(Figure 4a) and RLZ *k*-*ε* (Figure 4b) models on the horizontal plane at Z = 0.4H along the midline of the building model (Y = 0H). The results generated from the medium (M) and fine (F) mesh systems used in both models are very consistent. However, the differences between the coarse (C) mesh system and the other two mesh systems are quite obvious, particularly in the far windward and leeward regions. Apart from grid sensitively, Figure 4(b) presents that the RLZ *k*-*ε* model tends to overestimate the velocity ratio on the windward side and underestimates the velocity ratio in the leeward region of the building. The simulation results of the RLZ *k*-*ε* model also show greater deviations of velocity ratio in the building wake starting from X = 2.5H to X = 5.5H.

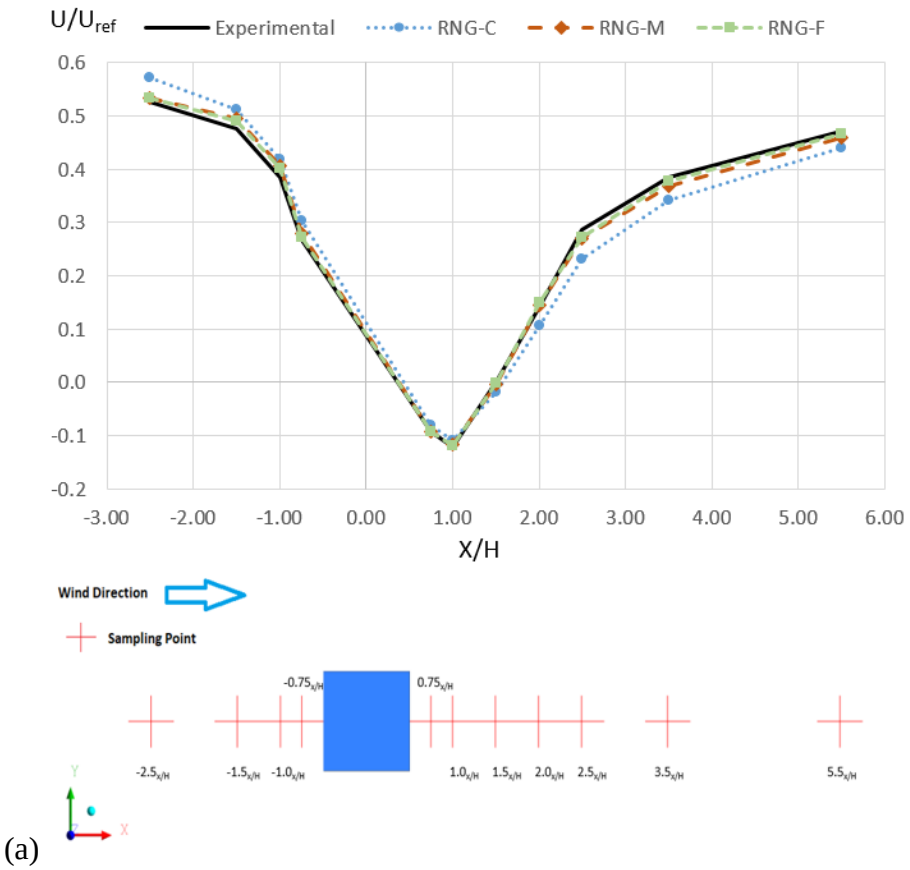

(a)

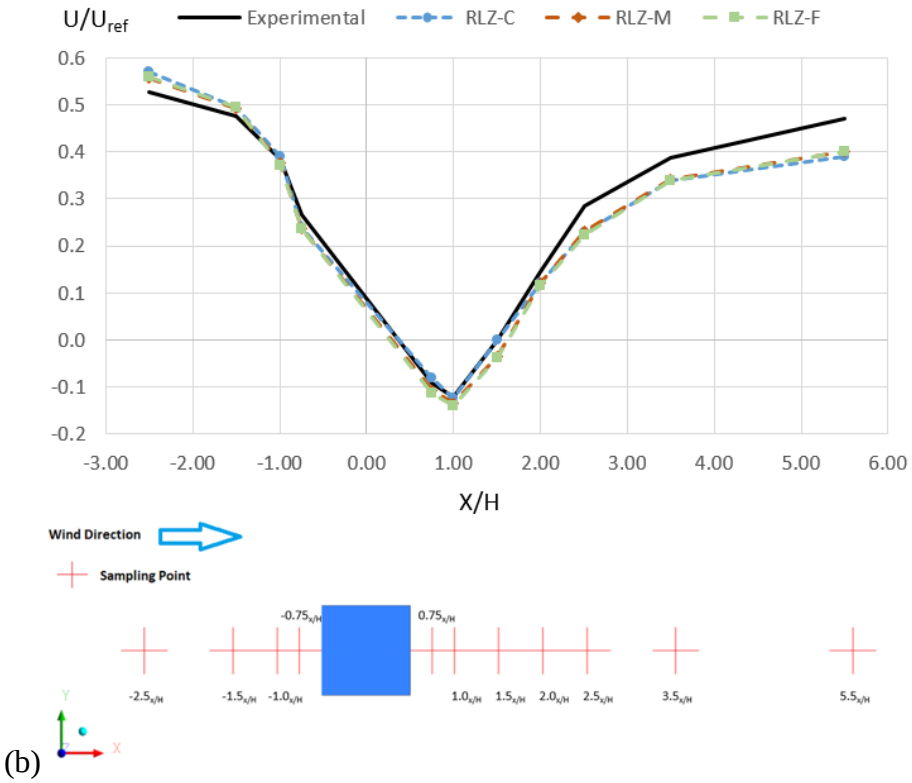

(b)

Figure 4. Comparison of the wind tunnel data with the simulated (a) RNG and (b) RLZ k-ε models with three mesh systems: coarse (C), medium (M), and fine (F).

Table 2 shows that the RNG *k*-*ε* model, in general, has a better performance statistically with the higher correlation coefficients (0.988 to 0.999) when compared with the RLZ *k*-*ε* model (0.988 to 0.992). Besides, the geometric median biases (MGs) of the results from the RNG *k*-*ε* model are closer to 1. As for the comparison amongst the three mesh systems, the medium mesh demonstrates similar results to the fine mesh system and performs much better than the coarse mesh in terms of the correlation coefficients. Therefore, the medium mesh system with the minimum grid size of 0.0002 m is sufficiently fine for the CFD simulation.

Table 2. Statistical test results of (a) RNG and (b) RLZ k-ε models with three mesh systems, namely coarse (C), medium (M), and fine (F).

(a)

Distance	U/U_{ref}			
(X/H)	Experimental	RNG-C	RNG-M	RNG-F
-2.50	0.526	0.573	0.533	0.533
-1.50	0.477	0.513	0.495	0.491
-1.00	0.385	0.419	0.407	0.401
-0.75	0.267	0.303	0.279	0.271
0.75	-0.092	-0.081	-0.092	-0.092
1.00	-0.122	-0.110	-0.117	-0.120
1.50	0.001	-0.019	-0.004	-0.001
2.00	0.144	0.108	0.146	0.149
2.50	0.285	0.231	0.270	0.273
3.50	0.386	0.341	0.368	0.379
5.50	0.471	0.440	0.459	0.468
Correlation Coefficient		0.988	0.998	0.999
Geometric mean biases (MG)		1.0	1.0	1.0

(b)

Distance	U/U_{ref}			
(X/H)	Experimental	RLZ-C	RLZ-M	RLZ-F
-2.50	0.526	0.571	0.557	0.560
-1.50	0.477	0.495	0.491	0.494
-1.00	0.385	0.390	0.376	0.372
-0.75	0.267	0.239	0.238	0.236
0.75	-0.092	-0.081	-0.106	-0.113
1.00	-0.122	-0.123	-0.135	-0.140
1.50	0.001	0.000	-0.036	-0.037
2.00	0.144	0.121	0.122	0.114
2.50	0.285	0.229	0.231	0.222
3.50	0.386	0.339	0.340	0.338
5.50	0.471	0.390	0.399	0.401
Correlation Coefficient		0.988	0.992	0.992
Geometric mean biases (MG)		1.1	1.1	1.1

Figure 5 illustrates the changes in velocity ratio at different locations along the y-axis direction of the model on two horizontal plains at Z = 0.4H and Z = 0.8H.

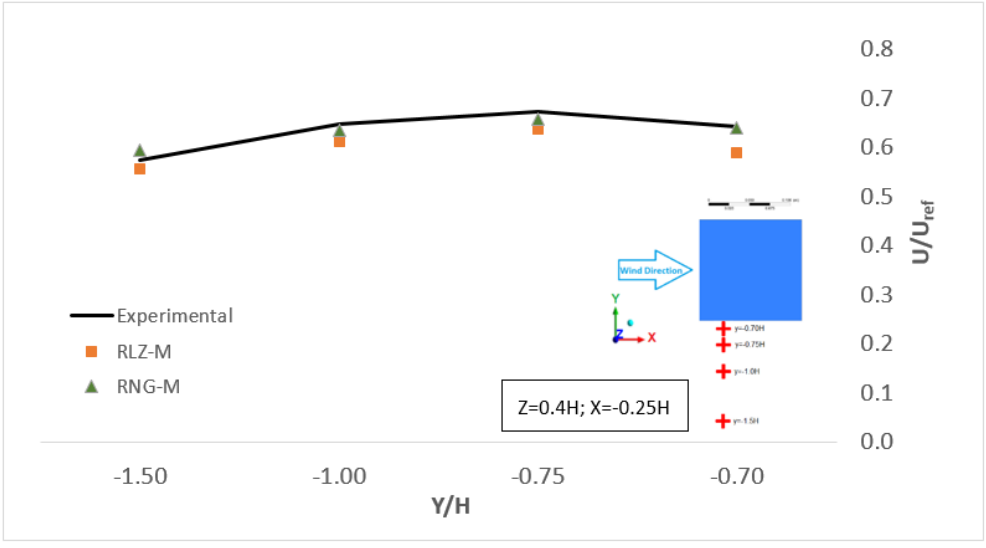

(a)

(b)

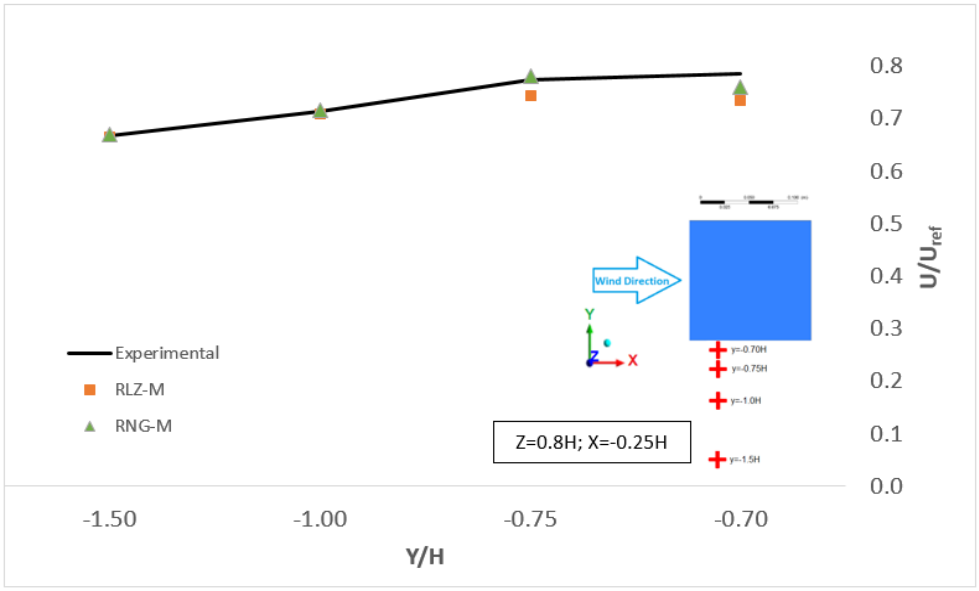

Figure 5. Comparison of the wind tunnel data with the simulated RNG and (b) RLZ k-ε models with the medium mesh system at two different horizontal levels: (a) Z = 0.4H, (b) Z = 0.8H. The red '+'s in the insets are the measurement points along the y-axis direction.

Figure 5 shows that both RNG and RLZ *k*-*ε* models show good agreement with the wind tunnel data, except for the sampling location near the lateral wall (Y = -0.7H) simulated by the RLZ *k*-*ε* model. Statistically, the RNG *k*-*ε* model performs better than the RLZ *k*-*ε* model with correlation coefficients ranging from 0.965 to 0.998, and MGs ranging from 1.003 to 1.005.

Figure 6 presents the comparison of wind tunnel data with the simulation data at different vertical distances expressed in Z/H near the windward (Figure 6a), leeward (Figure 6b), and lateral (Figure 6c) walls of the building. Figure 6a shows that on the windward side, the MGs between the wind tunnel data and those from the RLZ and RNG *k*-*ε* models are 1.073 and 1.035, respectively. On the leeward side (Figure 6b), the

MGs between the experimental data and those from the RLZ and RNG *k*-*ε* models are 1.145 and 1.098, respectively. The simulated and experimental wind velocity ratios on the lateral wall agree well (as shown in Figure 6c). The MGs between the experimental data and those from RLZ and RNG *k*-*ε* models are 1.100 and 1.069, respectively. However, the RLZ *k*-*ε* model underestimates the horizontal wind velocities at a higher vertical level, i.e., Z/H = 0.6-1.0, compared with its RNG counterpart.

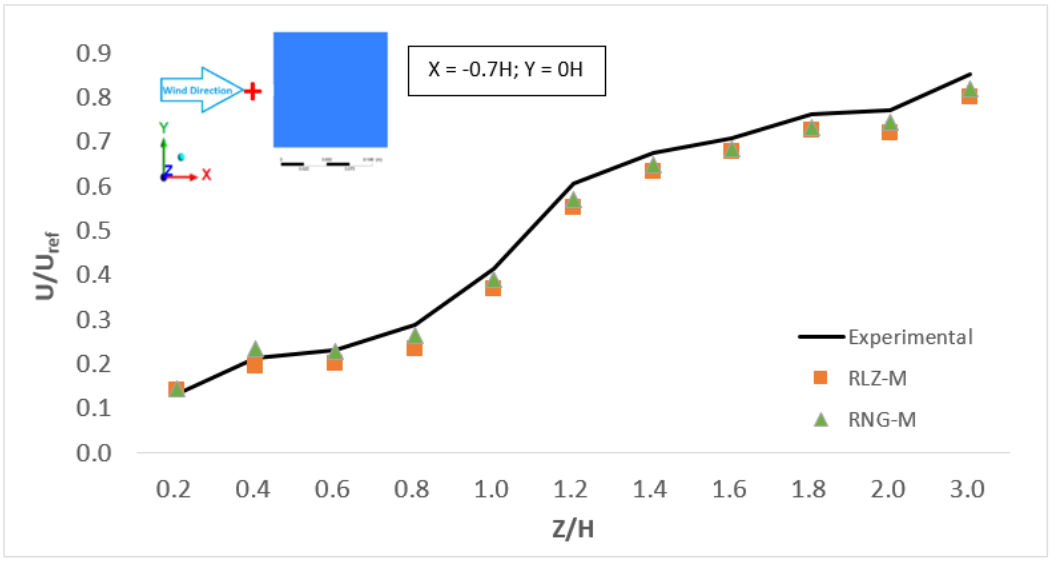

(a)

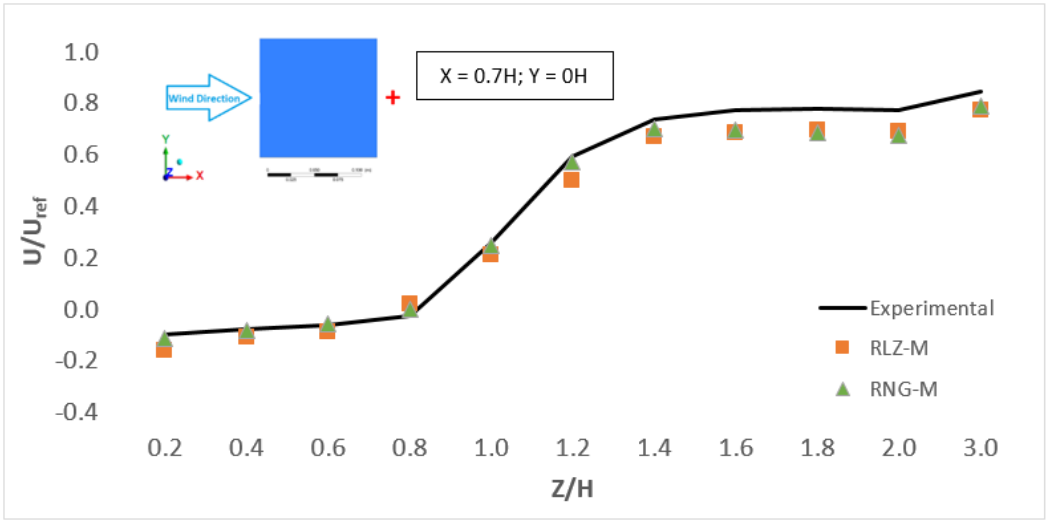

(b)

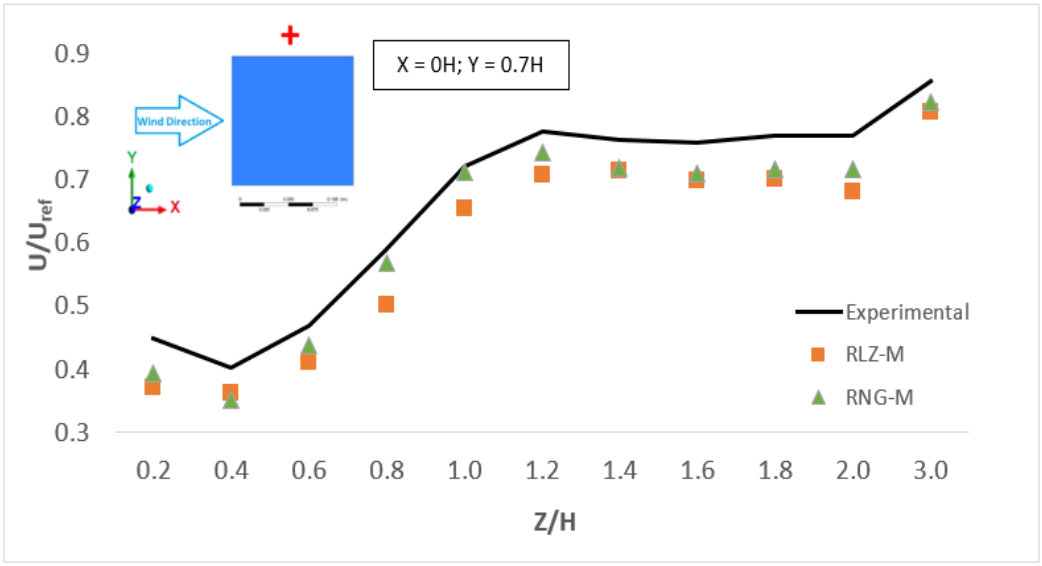

(c)

Figure 6. Comparison of the wind tunnel data with the simulated RLZ and RNG k-ε model results on the (a) windward; (b) leeward; and (c) lateral walls of the building block. The red '+' in the inset on the left upper corner is the measurement point. The building height fraction 'H' is represented on the x-axis.

After considering the overall performance of the two *k-ε* models, the RNG *k-ε* model with a medium mesh system was adopted in the current study, as it can economically provide sufficient accuracy for predicting the wind flow around an isolated building.

Description of building configurations

To study the effects of building configurations and incident wind angles on the airflow patterns around the building, a normal building configuration, i.e., "-"-shaped (Figure 7a) building, was constructed and used to compare with the two generic building configurations, i.e., "T"-shaped (Figure 7b) and "+"-shaped (Figure 7c) buildings. The effects of direct approaching (θ = 0˚) wind, oblique (θ = 45˚), oblique

opposing (θ = 135˚), lateral (θ = 90˚), and opposing (θ = 180˚) wind directions (see Figures 7a, b, and c) were investigated. The front and back sections of the buildings were also labelled for ease of reference and identification. The validated mesh, inflow wind profile, computational domain size, turbulence model, and numerical methods were used in this study used for the wind flow simulation around the buildings.

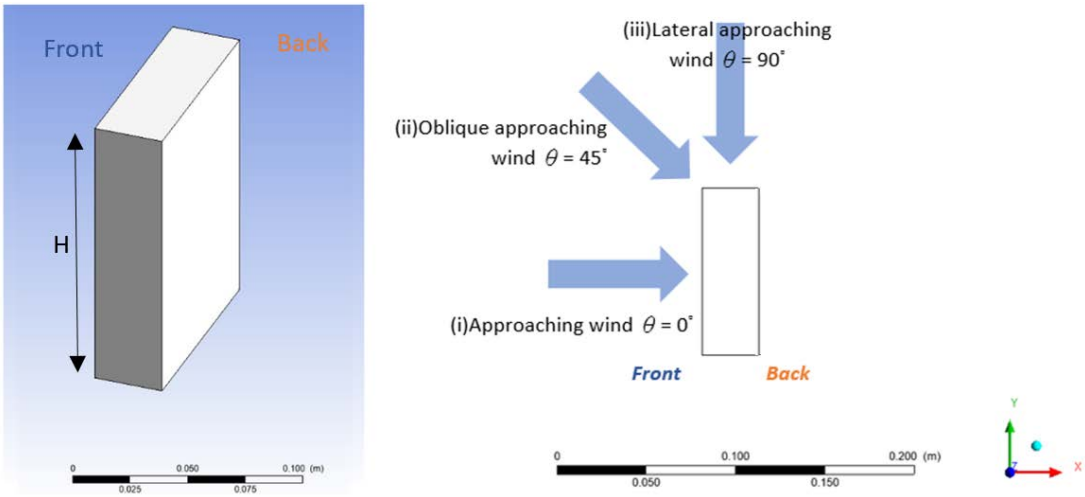

(a)

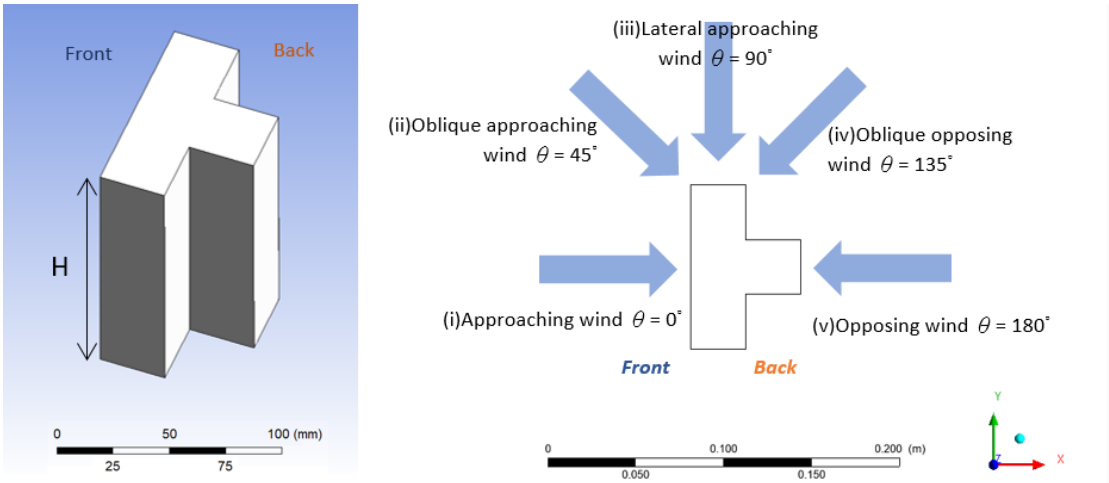

(b)

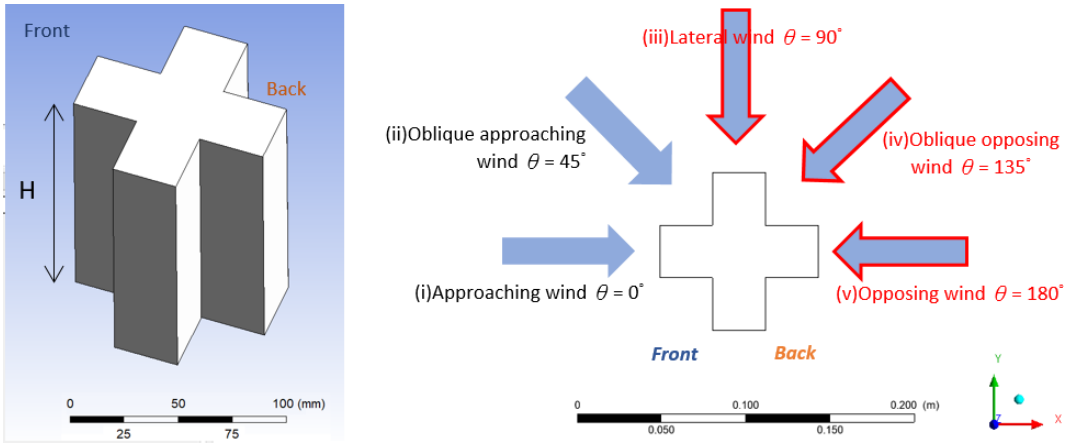

(c)

Figure 7. Building configurations and incident wind directions: (a) normal "-" – shaped building, (b) "T"-shaped building; (c) "+"-shaped building. H = 125 mm. In Figure 7(c), the wind angles in (iii) and (v) are equivalent to the wind angle shown in (i), and the effects of the wind angles shown in (ii) and (iv) are identical.

Because the wind flow in zones where the mean wind velocity ratio is less than 0.25 was deemed uncomfortable and unfavourable for pedestrian activities, the distributions of the mean wind velocity ratios at the pedestrian level (1.75 m at equivalent full scale) in the building wakes were calculated. Areas with a mean wind velocity ratio less than 0.25 would be regarded as low-wind velocity zones. Moreover, because units and windows along the leeward wall were considered less favourable in terms of fresh air intake and natural ventilation than those along the windward wall, the distributions of the dimensionless pressure coefficients (C_p) on the leeward surfaces ($C_P = (P - P_0)/(0.5\rho U_{ref}^2)$, where P is the static pressure, P_0 is the reference pressure, ρ is the density, and U_{ref} is the reference u-velocity) were calculated.

Results and discussions

The effects of wind direction on the flow patterns around the normal "-"-shaped building

The general features of the wind velocity ratio (U/U_{ref}) distribution around the normal building configuration, i.e., "-"-shape, at the pedestrian level (1.75 m) under different incident wind directions are shown in Figure 8. As shown, the three different wind directions, namely direct approaching (0°), oblique (45°), and lateral (90°) wind directions, have different velocity distribution patterns and low-wind velocity zone developments in the building wake.

(a)

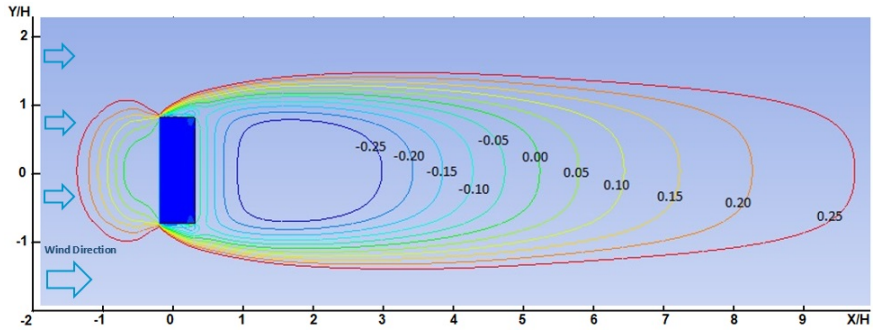

(b)

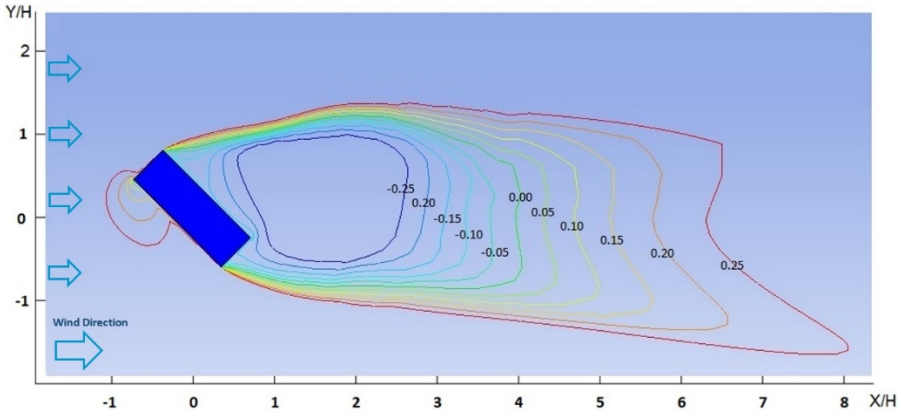

(c)

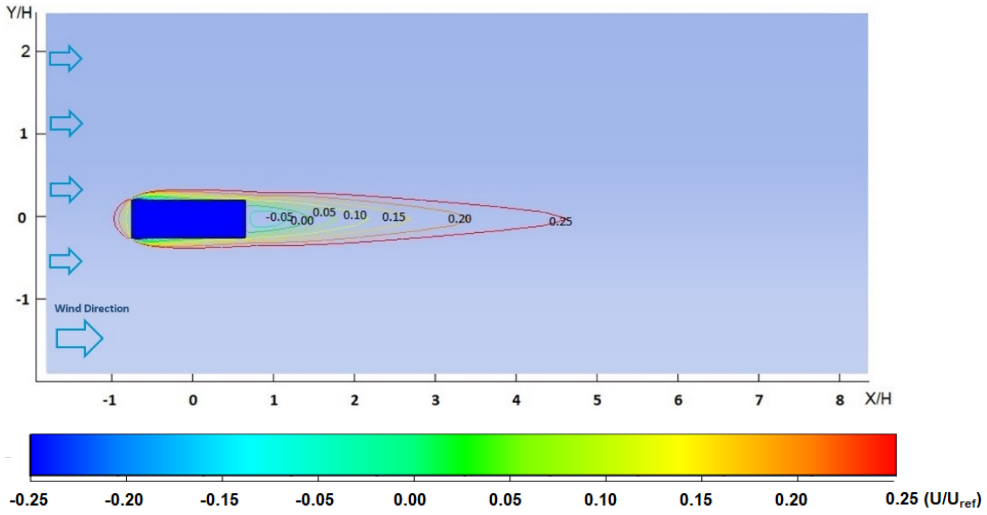

Figure 8. Distributions of U/U_{ref} in the horizontal plane at the pedestrian height (1.75 m) of the "-"-shaped building: (a) direct approaching wind $\theta = 0^{\circ}$; (b) oblique approaching wind $\theta = 45^{\circ}$; (c) lateral wind $\theta = 90^{\circ}$.

The low-wind velocity zone (i.e., $U/U_{ref} < 0.25$ where $U_{ref} = 6$ m/s) in the building wake of the lateral wind (90°) is the smallest (among those formed by the wind from the three wind directions) (see Figure 8c). This zone extends horizontally to 4.75 H downwind (x-axis direction) and has a maximum bilateral width of less than 0.7H (y-axis). That means the wind velocities in the wake under the lateral wind condition would be the highest among all wind directions. However, when the approaching wind is direct (0°), the low-wind velocity zone reaches the longest distance, when compared with other directions, at 9.75 H (x-axis) and has a maximum bilateral width of 3 H (y-axis) in the building wake. The downwind extension and maximum bilateral width of the low-wind velocity zone under the lateral wind (90°) are 329% and 105%, respectively, less than they are in the case of a direct approaching wind (0°), which is the worst-case scenario. In other words, the airflow in the building wake under a direct

approaching wind (0°) is relatively stagnant, and the wind environment in this area may not be favourable for pedestrian activities.

In the oblique wind condition (45°), a smaller low-wind velocity zone is noticed. The low-wind velocity zones along the x-axis direction extend to 8H (x-axis), and the bilateral width of 4 H along with the y-axis orientation. The gross area of the low-wind velocity zone in the building wake in the oblique wind case (45°) is still more extensive than in the case of the lateral wind angle (90°), and similar to having the direct approaching wind (0°). As such, the wind environment in the building wake under the oblique wind direction is still less favourable for pedestrian activities.

The effects of wind direction on the flow patterns around the "T"-shaped building

Figure 9 shows the general features of the wind velocity ratio (U/U_{ref}) distribution around the "T"-shaped building at the pedestrian level under different incident wind directions. As shown, the five prescribed wind directions have different velocity distribution patterns and low-wind zone developments in the building wake.

(a)

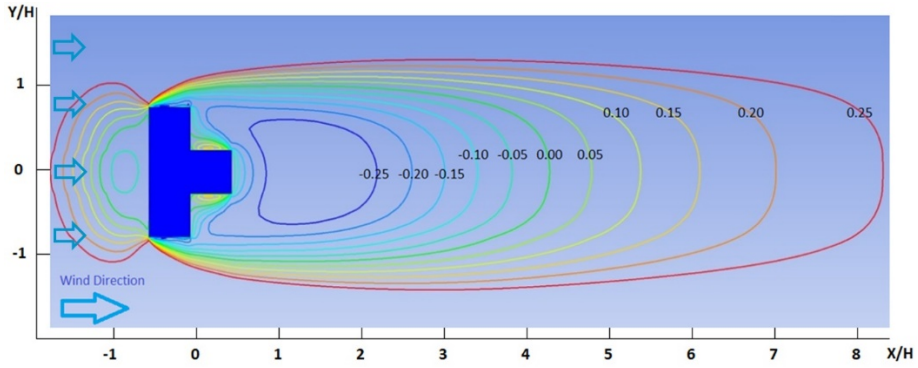
Y/H
1
0
-1
-0.25 -0.20 -0.15
-0.10 -0.05 0.00 0.05
0.10 0.15 0.20 0.25
Wind Direction
-1 0 1 2 3 4 5 6 7 8 X/H

(b)

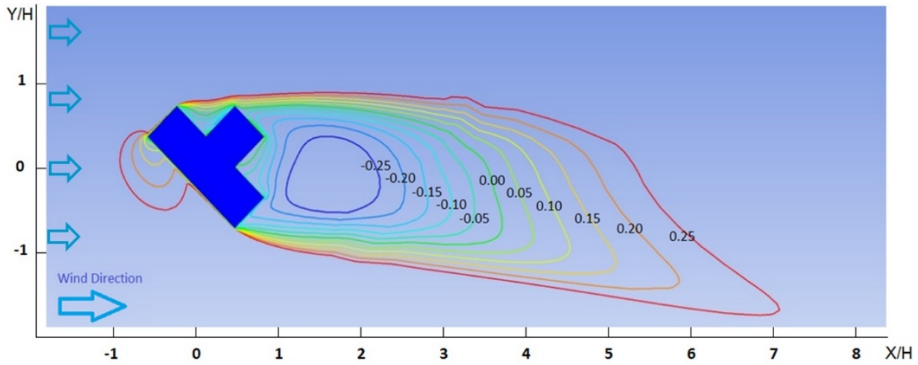
Y/H
1
0
-1
-0.25
-0.20
-0.15
-0.10
-0.05
0.00
0.05
0.10
0.15
0.20
0.25
Wind Direction
-1 0 1 2 3 4 5 6 7 8 X/H

(c)

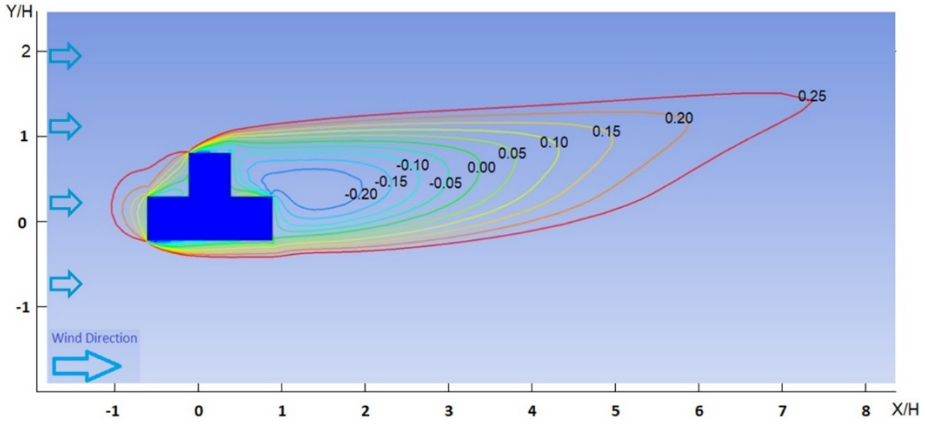
Y/H
2
1
0
-1
-0.20
-0.15
-0.10
-0.05
0.00
0.05
0.10
0.15
0.20
0.25
Wind Direction
-1 0 1 2 3 4 5 6 7 8 X/H

(d)

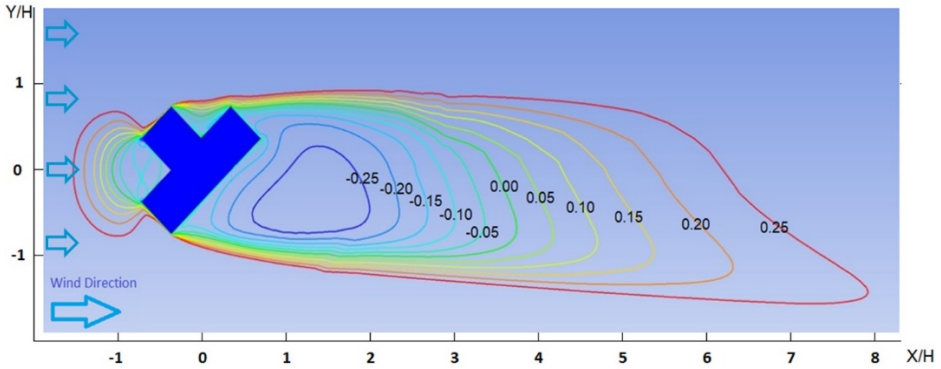
Y/H
1
0
-1
-0.25
-0.20
-0.15
-0.10
-0.05
0.00
0.05
0.10
0.15
0.20
0.25
Wind Direction
-1 0 1 2 3 4 5 6 7 8 X/H

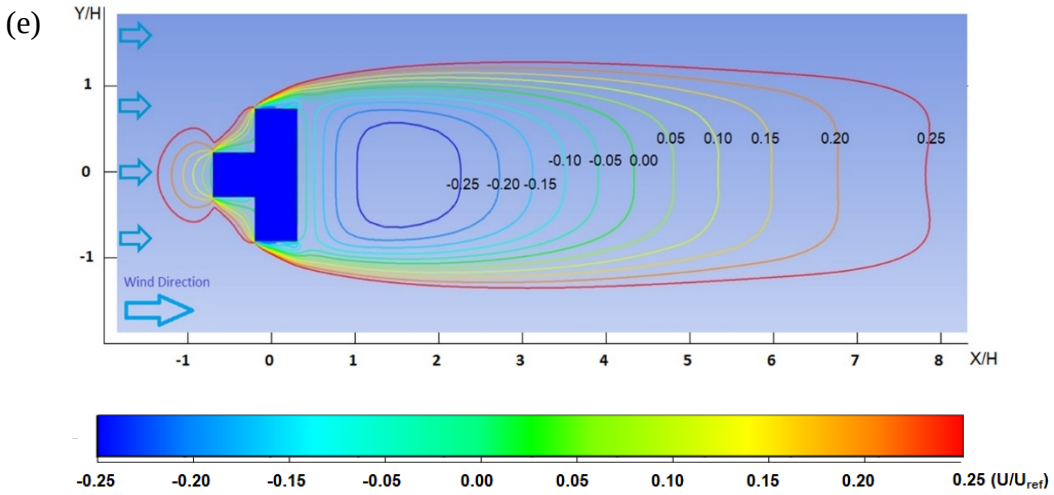

Figure 9. Distributions of U/U_{ref} in the horizontal plane at the pedestrian height (1.75 m) of the "T"-shaped building: (a) direct approaching wind θ = 0˚; (b) oblique approaching wind θ = 45˚; (c) lateral wind θ = 90˚; (d) oblique opposing wind θ = 135˚; (e) opposing wind θ = 180˚.

Referring to Figure 8 (for "-"-shaped building) and Figure 9 (for "T"-shaped building), the flow patterns and velocity distributions for direct approaching (0°) and oblique (45°) wind directions in both building configurations are very similar. Though they are similar in shape, the horizontal spread of the low-wind velocity zone developed in the building wake of the "T"-shaped building is 18% shorter than that of the "-"-shaped building. The bilateral spread of the low-wind velocity zone along the y-axis is 9.1% shorter than the "-"-shaped building. As for the oblique case (45°), the horizontal spread of the low-wind velocity zone developed in the building wake of the "T"-shaped building is 14.3% shorter than that of the "-"-shaped building. The bilateral width of the low-wind velocity zone along with the y-axis is 13% narrower than the "-"-shaped building. For the oblique opposing (135°) wind case in Figure 9d, where the front section (without the protruding structure) of the "T"-shaped building appears in the

wake, the horizontal spread of low-wind velocity zone developed in the building wake of the “T”-shaped building is same as the one developed in the “-”-shaped building. As air turbulence takes place and the vortex is developed around the corners of the protruding structure in the back section of the “T”-shaped building, it shortens the low-wind velocity zone development in the wake and reduces the size of the air stagnation zone at pedestrian level in the building wake.

For the lateral (90°) wind direction case, the low-wind velocity zone developed in the building wake of the “-” – shaped building in the lateral wind condition (90°) is a lot smaller than the one developed in the “T”-shaped building. However, the low-wind velocity zone in the building wake of the lateral (90°) wind is still the smallest (among those formed by the wind from the five prescribed wind directions) (see Figure 9c). This zone extends horizontally to 7.3 H downwind (x-axis direction) and has a maximum bilateral width of about 1.8 H (y-axis). When the approaching wind is direct (0°), the low-wind velocity zone reaches 8.25 H (x-axis) and has a maximum bilateral width of 2.9 H (y-axis) in the building wake. The downwind extension and maximum bilateral width of the low-wind velocity zone under the lateral wind (90°) are 11.5% and 37.9%, respectively, less than they are in the case of a direct approaching wind (0°), which is the worst-case scenario. The smallest zero-wind velocity zone (among those corresponding to the five prescribed incident wind angles) is observed under the lateral

wind: 3.4 H downstream extension (x-axis) and a maximum bilateral width of 1.25 H (y-axis). These dimensions are 20.9% and 37.5%, respectively, lower than the maximum reach of the zero-wind velocity zone in the downstream and bilateral directions under a direct approaching wind (0°). In other words, the airflow in the building wake under a direct approaching wind (0°) is relatively stagnant, and the wind environment in this area may not be favourable for pedestrian activities. The situation when the incident wind direction is 180° (see Figure 9e), i.e., when the wind is perpendicular to the back of the “T”-shaped building, is similar. The low-wind velocity area in the building wake is much larger under these wind conditions than in the lateral wind angle (90°) case. The zero-wind velocity zone (when the incident wind direction is 180°) extends to around 4.3H (x-axis) downstream and covers a broader bilateral region of about 2H (y-axis). The area of the low-wind velocity zone (in the lateral wind case) is similar to that of the zone formed by the direct wind: it extends horizontally to near 8H (x-axis) downstream and covers the bilateral region of 2.65H (y-axis) in the building wake.

The two oblique winds (45° and 135°) produce smaller low-wind velocity zones than the direct approaching (0°) and opposing (180°) wind conditions. The low-wind velocity zones along the x-axis direction extend to 7H (x-axis) and 8H (x-axis) downstream, respectively, in the oblique (45°) and oblique opposing (135°) wind cases.

Again, it is worth noting that when the protruding back section of the building appears as the leeward wall in the oblique (45°) wind case, the development of the low-wind velocity zone would be shortened. It may be contributed by the vortex formation around the corners of the protruding structure on the leeward wall under the oblique (45°) wind direction. Besides, both oblique cases show a shorter zero-wind velocity flow distance of 3.6H (x-axis) and a narrower bilateral reach of 1.65H and 1.7H (y-axis) when compared with horizontal and bilateral extensions in the direct approaching (0°) and opposing wind (180°) cases. However, the gross area of the low-wind velocity zone in the building wake in the two oblique wind cases is still larger than it is in the case of the lateral wind angle (90°). Therefore, the wind environment in the building wake is still less favourable for pedestrian activities.

The effects of wind directions on the "+"-shaped building

The "+"-shaped building is horizontally and bilaterally symmetrical. Hence, only two wind directions were modelled and studied, i.e., the direct approaching (analogous to the lateral and opposing wind directions) and oblique approaching (analogous to the oblique opposing) wind directions. Figure 10 shows that the area of the low-wind velocity zone developed in the building wake under oblique wind conditions, i.e., 45° and 135°, is smaller than it is under direct approaching (0°), lateral (90°), and opposing (180°) wind conditions.

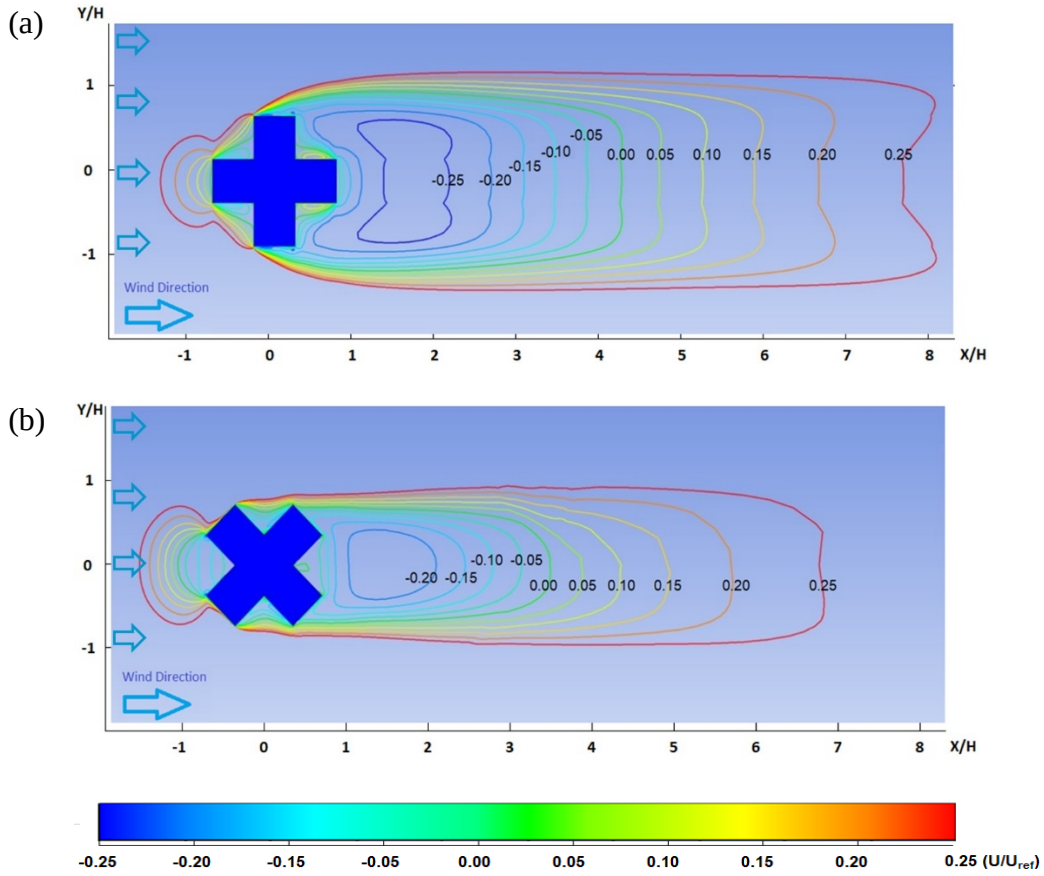

Figure 10. Distributions of U/U_{ref} in the horizontal planes at a pedestrian height (1.75 m at equivalent full scale) of a "+"- shaped building with (a) direct approaching wind angle: $\theta = 0^{\circ}$ (also includes 90˚ and 180˚); (b) oblique approaching wind angle: $\theta = 45^{\circ}$ (also includes 135˚).

When the incident wind is oblique (45°), the low-wind velocity zone extends horizontally to 6.8H (x-axis) downstream and has a maximum bilateral reach of only 1.9H (y-axis) (see Figure 10b). Its length and width are 15.0% and 30.9%, respectively, smaller than those of the low-wind velocity zones in the direct, lateral, and opposing direction cases, where the downstream reach of the low-wind velocity zone is 8H (x-axis), and the maximum bilateral reach is 2.75 H (y-axis). The zero-wind velocity zone in the oblique wind case extends to 3.5H (x-axis) downstream and bilaterally to 1.3H

(y-axis). However, under direct (0°), lateral (90°), and opposing (180°) wind conditions (see Figure 10a), the zero-wind velocity zone reaches 4.3H (x-axis) downstream and 1.75H along the y-axis. That means there is less airflow in the building wakes under these wind directions, and it is less comfortable for pedestrian activities. In the simulation of "+"-shaped building, the protruding structure in the back section of the building appears on the leeward in both direct (0°) approaching wind and oblique (45°) wind direction cases. As observed, the air turbulence developed near the protruding structure on the leeward wall would shorten the distance and horizontal spread of the low-wind velocity zone in the building wake. From Figures 9 and 10, the low-wind velocity zone developed in the oblique case (45°) would be shorter than the one with direct (0°) approaching wind direction. Hence, the airflow pattern in the building wake with this building configuration would create a smaller air stagnation zone and would be a more preferable outdoor condition for the pedestrians.

Figure 11 illustrates the airflow pattern on the median plane of the normal building configuration, i.e., "-"-shaped building, and the distributions of air pressure (C_p) on the windward and leeward walls under the prescribed incident wind angles.

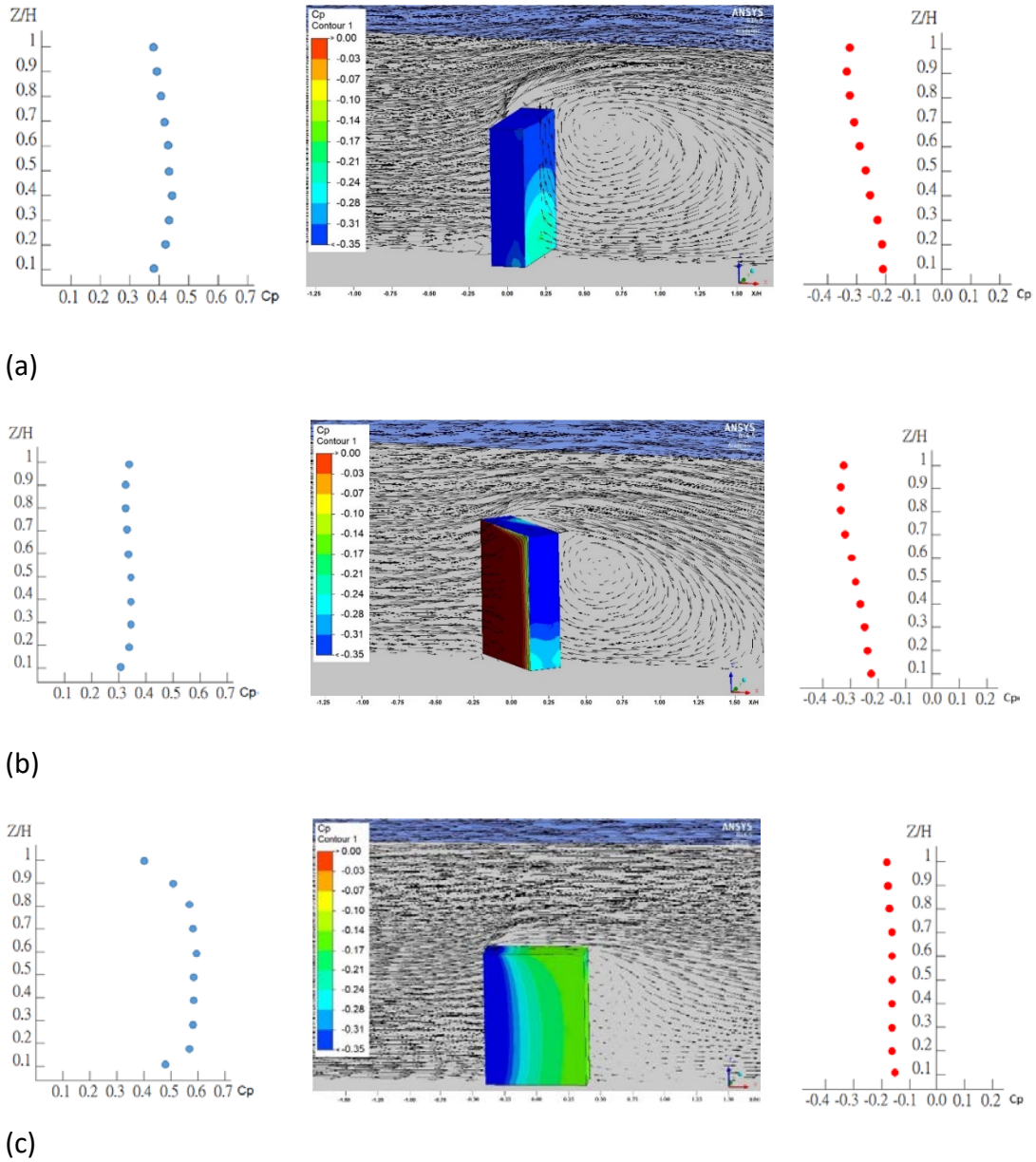

Figure 11. The distribution of pressure and airflow pattern at different height fractions (H = 125 mm) on the surface wall of the "-"-shaped building under three different incident wind directions: (a) approaching wind θ = 0˚; (b) oblique approaching wind θ = 45˚; (c) lateral wind θ = 90˚.

In general, the backflow of air occurs at the lower vertical levels or floors on the leeward wall of the building, and the flow separation creates an underpressure zone that enhances fresh air intake and drives natural ventilation of the building with windows installed on the leeward wall. This phenomenon becomes more noticeable in the direct

approaching (0°), where horizontal air movement on the leeward wall only occurs at the lower level of the building (see Figure 11a). For the lateral (90°) wind direction case, the vortex in the building wake was not complete, and the underpressures developed on the leeward wall are relatively consistent in different vertical distances of the building (see Figure 11c). The backflow of air takes place equally on the leeward wall. From Figure 11, one sees that when the air current flows back onto the lower part of the leeward wall, it moves upward, causing an uplift of air from the mid-level of the building to the roof. Though the underpressure becomes more substantial on the upper level, the vertical movement of airflow dominates the horizontal one. It creates less favourable wind conditions for mid to upper floors, where the wind velocity is significantly reduced.

Figure 12 shows the pressure coefficients along the leeward wall of the building under different incident wind directions. In general, the air pressure on the lower levels of the building is higher than on the middle and upper floors in different wind directions. In both direct approaching and oblique wind cases, it shows a relatively profound decrease of pressure coefficients on the leeward wall from Z/H 0.1 to Z/H 0.8. The upward pulling force, in the direct approaching (0°) and oblique (45°) wind cases, dominates, and hence diminishes the fresh air intake on the upper floors. It could weaken the benefit of natural ventilation through the windows on the leeward wall. In

contrast, the pressure drops in the lateral (90°) case are relatively steady along the vertical height on the leeward walls. The variations of wind flow on different vertical levels on the leeward wall are diminutive.

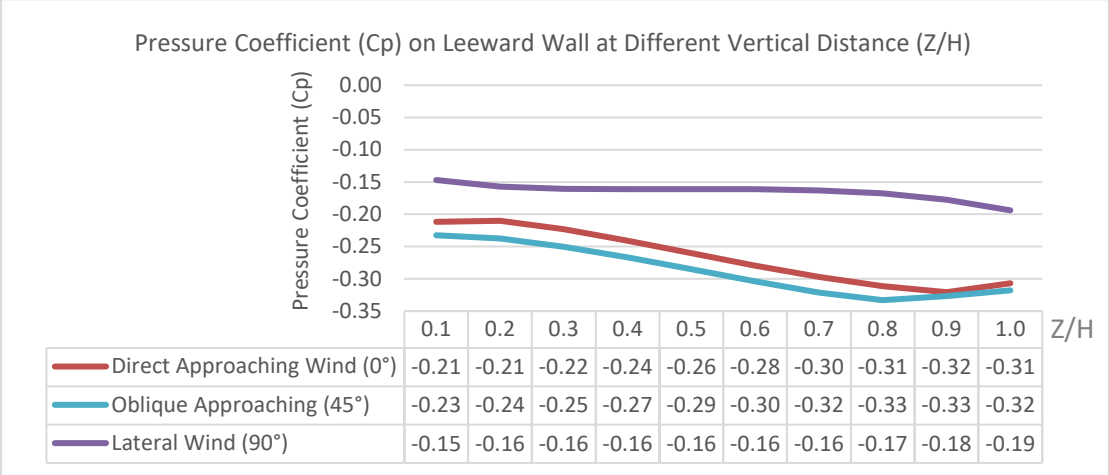

	0.1	0.2	0.3	0.4	0.5	0.6	0.7	0.8	0.9	1.0
Z/H										
Direct Approaching Wind (0°)	-0.21	-0.21	-0.22	-0.24	-0.26	-0.28	-0.30	-0.31	-0.32	-0.31
Oblique Approaching (45°)	-0.23	-0.24	-0.25	-0.27	-0.29	-0.30	-0.32	-0.33	-0.33	-0.32
Lateral Wind (90°)	-0.15	-0.16	-0.16	-0.16	-0.16	-0.16	-0.16	-0.17	-0.18	-0.19

Figure 12. The distribution of the pressure coefficient (C_p) at different height fractions (H=125 mm) on the leeward wall of the "-"-shaped building under different incident wind angles.

Figure 13 illustrates the airflow pattern on the median plane of the "T"-shaped building and air pressure distributions on the windward and leeward walls under the prescribed incident wind angles. Again, the backflow of air takes place at the lower vertical level or floors on the leeward wall of the building, and the flow separation creates an underpressure zone that enhances fresh air intake and drives natural ventilation of the building with windows installed on the leeward wall. This phenomenon becomes more noticeable in the direct approaching (0°) and opposing (180°) wind direction cases, where horizontal air movement on the leeward wall only occurs at the lower level of the building. From the diagrams in Figure 13, one sees that

when the air current flows back onto the lower part of the leeward wall, it moves upward, causing an uplift of air from the mid-level of the building to the roof. Though the underpressure becomes more substantial on the upper level, the vertical movement of airflow dominates the horizontal one. It creates less favourable wind conditions for mid to upper floors, where the wind velocity is considerably reduced.

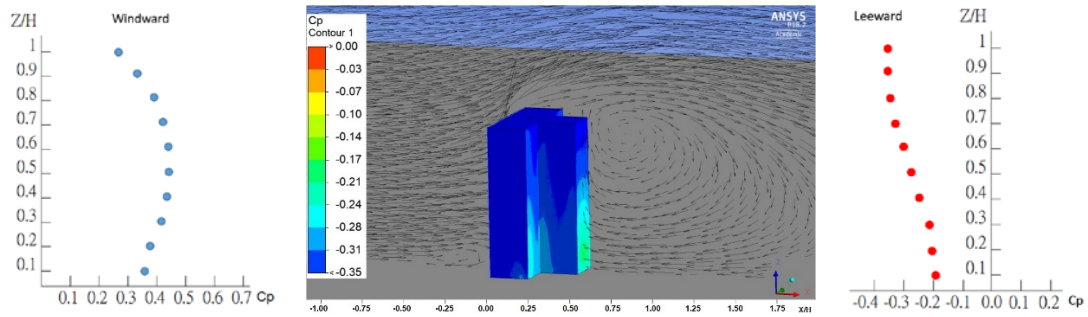

(a)

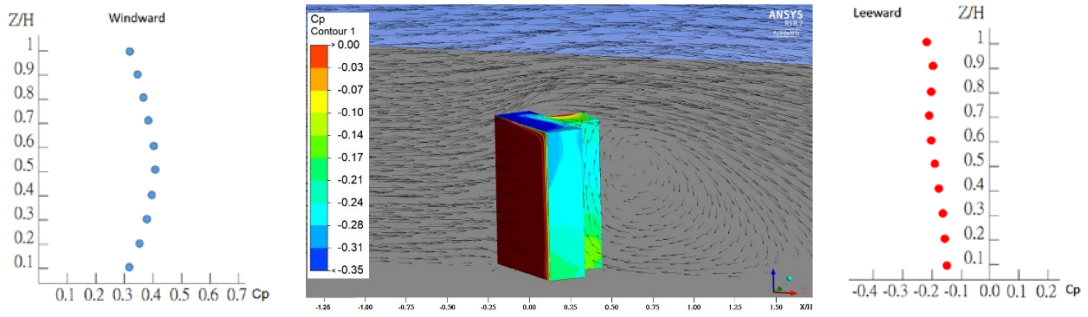

(b)

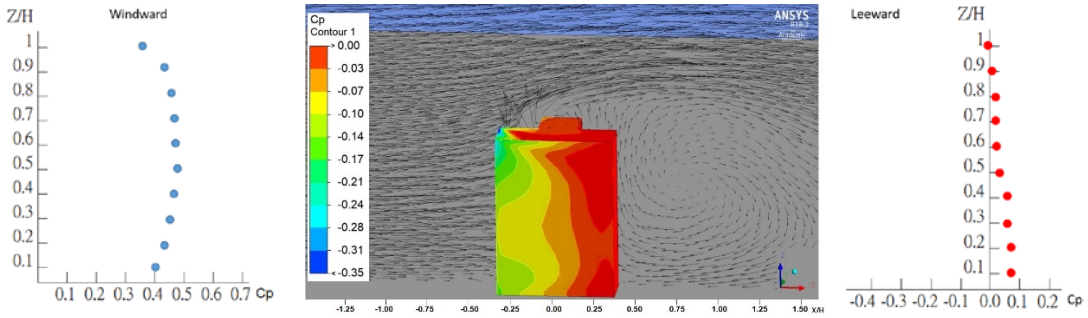

(c)

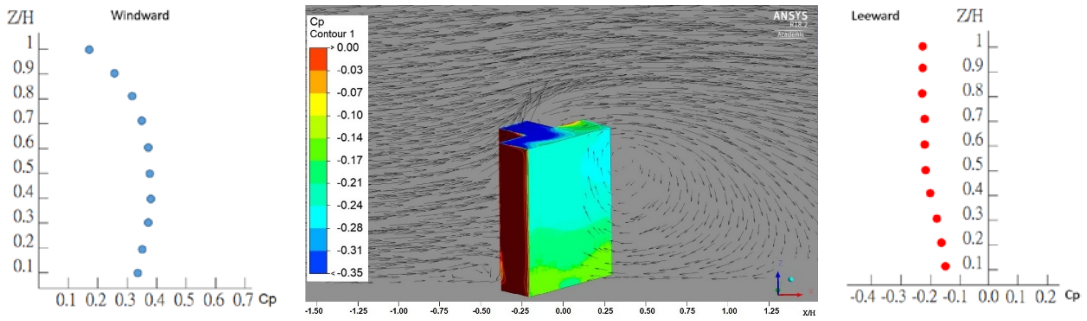

(d)

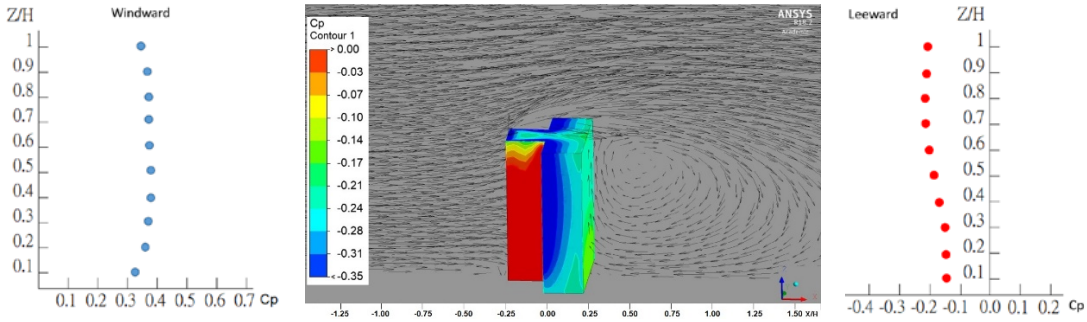

(e)

Figure 13. The distribution of pressure and airflow pattern at different height fractions (H=125 mm) on the surface wall of the "T"-shaped building under five different incident wind directions: (a) approaching wind θ = 0˚; (b) oblique approaching wind θ = 45˚; (c) lateral wind θ = 90˚; (d) oblique opposing wind θ = 135˚; and (e) opposing wind θ = 180˚.

The pressure coefficient (C_p) contours in Figure 13 also demonstrate the change of air pressure imposed on the leeward wall of the building under different wind direction situations. It is shown that the decreasing trend of C_p on the leeward wall in the direct approaching wind case (see Figure 13a) is more drastic when comparing with the other wind angle cases. This is quite similar to the development in the “-”-shaped building as shown in Figure 11. This implies a more potent upward pulling force of air in the leeward, and it further reduces horizontal air movement that allows air to infiltrate

the leeward wall on the upper floors.

Figure 14 shows the pressure coefficient along the leeward wall of the building under different incident wind directions. The air pressure on the lower levels of the building is generally higher than on the middle and upper floors in all the five prescribed wind directions. The direct approaching wind case shows a relatively profound decrease of pressure coefficients on the leeward wall from Z/H = 0.2 to Z/H = 0.8. In contrast, the pressure drops in oblique (45°), lateral (90°) and opposing (180°) wind angles are gradual along with the vertical height on the leeward walls. In the direct approaching (0°) wind case, the upward pulling force dominates and diminishes the fresh air intake on the upper floors. It could weaken the benefit of natural ventilation through the windows on the leeward wall.

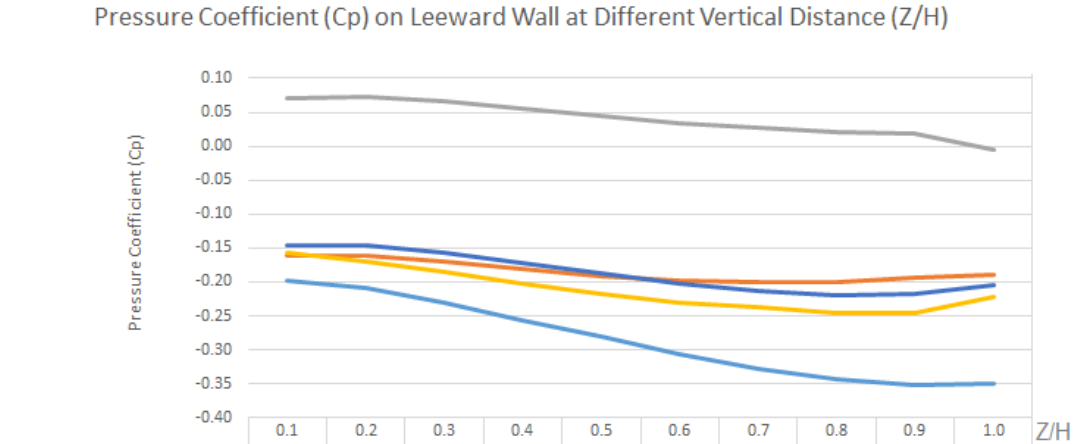

Z/H	0.1	0.2	0.3	0.4	0.5	0.6	0.7	0.8	0.9	1.0
Direct Approaching (0°)	-0.20	-0.21	-0.23	-0.26	-0.28	-0.31	-0.33	-0.34	-0.35	-0.35
Oblique Approaching (45°)	-0.16	-0.16	-0.17	-0.18	-0.19	-0.20	-0.20	-0.20	-0.19	-0.19
Lateral Wind (90°)	0.07	0.07	0.07	0.06	0.04	0.03	0.03	0.02	0.02	0.00
Oblique Opposing (135°)	-0.16	-0.17	-0.18	-0.20	-0.22	-0.23	-0.24	-0.25	-0.24	-0.22
Opposing Wind (180°)	-0.15	-0.15	-0.16	-0.17	-0.19	-0.20	-0.21	-0.22	-0.22	-0.20

Figure 14. The distribution of the pressure coefficient (Cp) at different height fractions (H = 125 mm)

on the leeward wall of the “T”-shaped building under different incident wind angles.

Figure 15 illustrates the airflow pattern along the median plane of the “+”-shaped building and the distributions of air pressure on the leeward wall under different incident wind angle conditions. Same as the "T"-shaped building, the backflow of air occurs outside the windows of the rooms on the lower level along the leeward wall of the building facilitates fresh air intake and natural ventilation. However, the horizontal air movement in the leeward only takes place outside the units on the lower level of the building. An upward movement of air from the mid-level of the building to the roof creates less favourable conditions for units on the mid to upper levels of the building due to reduced horizontal wind velocity. The pressure coefficient contours shown in Figure 15 also show the variations in air pressure imposed on the leeward wall of the building under different incident wind angles. Like the “-” and “T”-shaped building configurations, the decrease in C_p along the vertical height of the leeward wall is more noticeable in the direct approaching (0°) wind case. As a result, units on the upper floors in the leeward would have less natural ventilation.

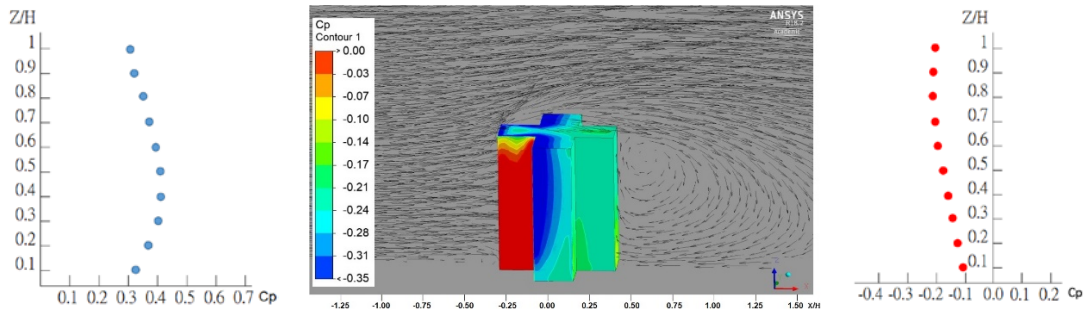

(a)

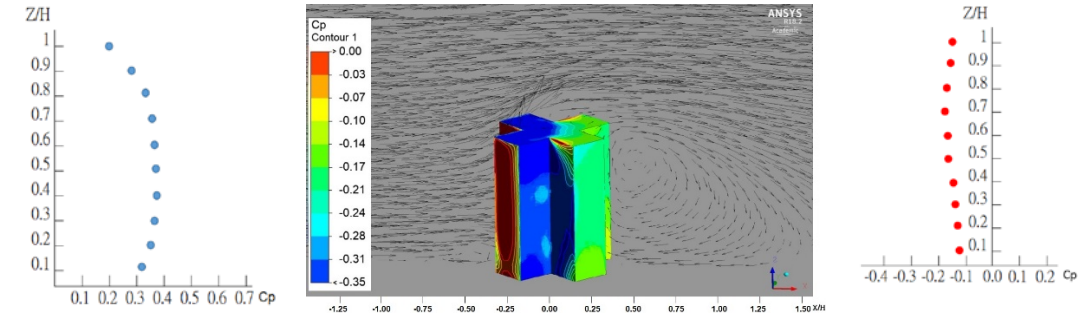

(b)

Figure 15. The distribution of pressure and airflow patterns at different height fractions (H = 125 mm) on the surface wall of the "+"-shaped building under two wind directions: (a) direct approaching wind angle: θ = 0˚ (also includes 90˚ and 180˚); (b) oblique approaching wind angle: θ = 45˚ (also includes 135˚)

In Figure 16, the C_p along the leeward wall of the building under different incident wind directions is plotted. The air pressures exerted on the leeward division of the building under the direct approaching (0°), lateral (90°), and opposing (180°) wind angles are lower than they are in the oblique wind angle (45° and 135°) cases. Therefore, units having windows on the leeward wall have better natural ventilation when the wind is blowing from oblique angles. Besides, the air pressure outside the lower level windows is higher than outside the middle and the upper floor windows under all the prescribed wind conditions. The pressure drops gradually with heights and increases

again at 0.7 and 0.8H (first upper-level floor). Therefore, units on the lower floor with windows on the leeward wall (particularly under the oblique wind conditions) experience better air intake and natural ventilation than the other units in the "+"-shaped building. However, an upward vertical movement of air again diminishes the benefit of natural ventilation through the windows of the units on the upper levels along the leeward wall.

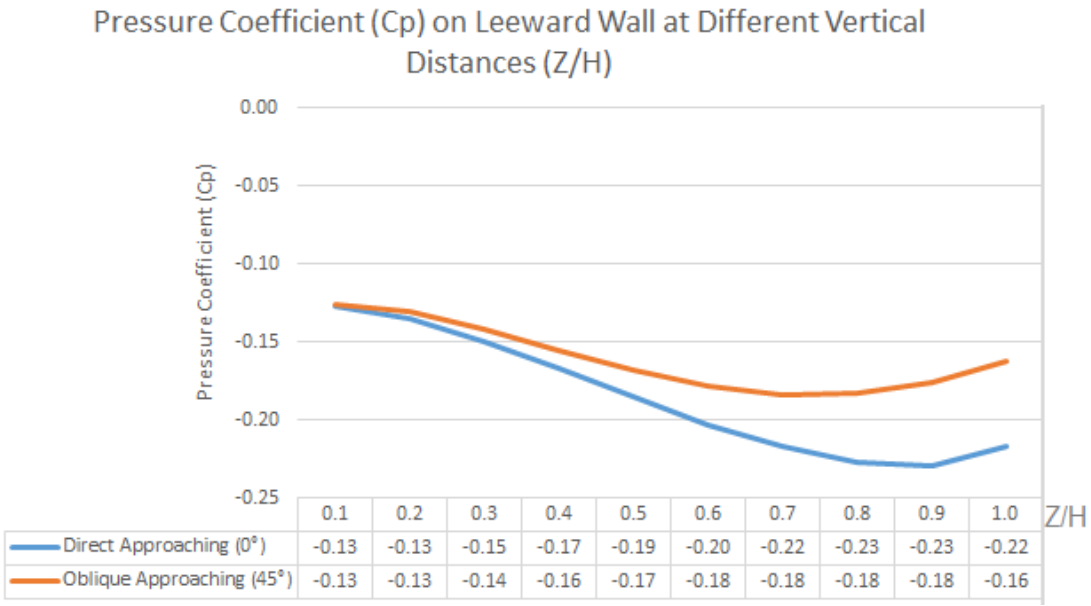

	0.1	0.2	0.3	0.4	0.5	0.6	0.7	0.8	0.9	1.0
Direct Approaching (0°)	-0.13	-0.13	-0.15	-0.17	-0.19	-0.20	-0.22	-0.23	-0.23	-0.22
Oblique Approaching (45°)	-0.13	-0.13	-0.14	-0.16	-0.17	-0.18	-0.18	-0.18	-0.18	-0.16

Figure 16. The pressure coefficient at different heights on the median line on the leeward wall of the “+”-shaped building under two wind conditions: (a) direct approaching wind angle: θ = 0˚ (also includes 90˚ and 180˚); (b) oblique approaching wind angle: θ = 45˚ (also includes 135˚)

Limitations and future research

The main goals of this study were to evaluate the impacts of different incident wind directions and building orientation on both the wind velocities at the pedestrian level in the building wake and the distribution of air pressure on the leeward walls of two

buildings. Two common building configurations were assumed. The simulation on a simple isolated building helps clarify the role of the building configurations and wind directions on the distribution of airflow in the wakes and the ventilation conditions on the leeward wall of the building. It is commonly used to test the accuracy of the model with experimental wind tunnel test results, and it helps provide inlet boundary conditions under homogenous atmospheric boundary layer for the simulation of the atmospheric boundary layer flow. However, only the changes in the flow fields in the building wakes and on the leeward sides of the buildings were studied. Other buildings or structures in close proximity can also have a significant effect on the ventilation flowing through the building. As such, the impacts of surrounding buildings or other structures that are a part of the urban environment on the ventilation of the building and dispersion of pollutants outside the buildings will be assessed in future studies. Simulations will be performed to resolve the effects of different building arrays and configurations on the flow fields, and the interference effect of surrounding environments on the pressure distributions along building walls will be identified. As isothermal conditions are assumed in this study, non-isothermal conditions will be assumed in future studies, and the effects of temperature gradients and convective heat transfer on the ventilation inside the building will be considered. Finally, the balance

between wind and buoyancy as driving forces for the inside airflow will be addressed in future research.

Conclusion

In this study, simulation results showed that the incident wind angle and building orientations of "T"-and "+"-shaped buildings, configurations common in Hong Kong, have a substantial effect on the low-wind velocity zone development in the wakes and the pressure distributions on the leeward walls of the buildings when compared with the normal building configuration, “-”-shaped building. For "T"-shaped building, five incident angles were considered: direct approaching (0°), oblique approaching (45°), lateral (90°), oblique opposing (135°), and opposing (180°) wind angles. For "+"-shaped building, there were two: direct (0°) and oblique (45°).

To conclude, incident wind directions and building configurations have significant effects on the ventilation of an urban setting and the air qualities in outdoor and indoor environments. First, when the wind is blowing from an oblique (45°) angle or onto a lateral side (90°) of a “T”-shaped or “+”-shaped building, the horizontal distance between the building and the low-wind velocity zone in its wake is the smallest, and the air velocity in the building wake is the highest. Second, the vortex formed near the protruding structure in the back section on the leeward of the building could help

shorten the horizontal spread of zero-velocity and low-wind velocity zone in the building wake. The resulting high-velocity flow on the leeward side can penetrate more deeply into the street canyon and facilitate the dispersion of air pollutants in the building wake. This would provide a more favourable outdoor wind condition for pedestrians to enjoy outdoor activities in the building wake region. Third, natural ventilation through the windows due to the pressure differences on the leeward wall of the building can also help improve the indoor environment. However, the upward air movement in the upper part of the leeward wall is noticeable and dominating under all incident wind directions. This effect diminishes the benefit of natural ventilation of units on the upper floors through their leeward windows. The ventilation force on the leeward wall is the highest when the lateral wind is dominating, while the C_p values of the leeward walls in all other wind directions are noticeably much lower. The direct approaching (0°) wind case demonstrates the worst-case scenario in terms of the low airflow in the wake and the poor infiltration of air on the leeward wall, particularly on the upper floors. Taking the above observations into considerations, architects or building engineers need to consider the building shapes and orientations to enhance the wind comfort experienced by the pedestrian in the building wakes and the fresh air intake through the windows designed and installed on the leeward wall of the buildings adopting natural ventilation.

Acknowledgment

This research was not supported by any grants from funding agencies in the public, commercial, or not-for-profit sectors.

Author Contribution Statement:

Kai Yip Lee: conceptualization, methodology, simulation, formal analysis, investigation, writing – original draft.

Cheuk Ming Mak: conceptualization, methodology, investigation, resources, writing – review and editing, supervision.

Declaration of Conflict of Interests

The author(s) declared no potential conflicts of interest with respect to the research, authorship, and/or publication of this article.

Reference

1. Borrego C, Martins H, Tchepel O, Salmim L, Monteiro A and Miranda AI. How urban structure can affect city sustainability from an air quality perspective. *Environmental Modelling and Software* 2006; 21: 461-467. DOI: 10.1016/j.envsoft.2004.07.009.

2. Lee KY and Mak CM. A comprehensive approach to study stack emissions from a research building in a small urban setting. *Sustainable Cities and Society* 2019; 51: 101710. DOI: https://doi.org/10.1016/j.scs.2019.101710.

3. Yuan C, Ng E and Norford LK. Improving air quality in high-density cities by understanding the relationship between air pollutant dispersion and urban morphologies. *Building and Environment* 2014; 71: 245-258. DOI: 10.1016/j.buildenv.2013.10.008.

4. Dai Y, Mak CM, Ai Z and Hang J. Evaluation of computational and physical parameters influencing CFD simulations of pollutant dispersion in building arrays. *Building and Environment* 2018; 137: 90-107. DOI: 10.1016/j.buildenv.2018.04.005.

5. Ai ZT and Mak CM. CFD simulation of flow in a long street canyon under a perpendicular wind direction: Evaluation of three computational settings. *Building and Environment* 2017; 114: 293-306. DOI: 10.1016/j.buildenv.2016.12.032.

6. Chew LW and Norford LK. Pedestrian-level wind speed enhancement in urban

street canyons with void decks. *Building and Environment* 2018; 146: 64-76. DOI: https://doi.org/10.1016/j.buildenv.2018.09.039.

7. Du Y, Mak CM, Liu J, Xia Q, Niu J and Kwok KCS. Effects of lift-up design on pedestrian level wind comfort in different building configurations under three wind directions. *Building and Environment* 2017; 117: 84-99. DOI: https://doi.org/10.1016/j.buildenv.2017.03.001.

8. Du Y, Mak CM, Kwok K, Tse K-T, Lee T-c, Ai Z, Liu J and Niu J. New criteria for assessing low wind environment at pedestrian level in Hong Kong. *Building and Environment* 2017; 123: 23-36. DOI: https://doi.org/10.1016/j.buildenv.2017.06.036.

9. Ng E. Policies and technical guidelines for urban planning of high-density cities – air ventilation assessment (AVA) of Hong Kong. *Building and Environment* 2009; 44: 1478-1488. DOI: https://doi.org/10.1016/j.buildenv.2008.06.013.

10. Chen KW and Norford L. Evaluating Urban Forms for Comparison Studies in the Massing Design Stage. *Sustainability* 2017; 9: 987.

11. Huang Y, Hu X and Zeng N. Impact of wedge-shaped roofs on airflow and pollutant dispersion inside urban street canyons. *Building and Environment* 2009; 44: 2335-2347. DOI: https://doi.org/10.1016/j.buildenv.2009.03.024.

12. Yim SHL, Fung JCH, Lau AKH and Kot SC. Air ventilation impacts of the "wall effect" resulting from the alignment of high-rise buildings. *Atmospheric Environment*

2009; 43: 4982-4994. Article. DOI: 10.1016/j.atmosenv.2009.07.002.

13. Mittal H, Sharma A and Gairola A. Numerical simulation of pedestrian level wind flow around buildings: Effect of corner modification and orientation. *Journal of Building Engineering* 2019; 22: 314-326. DOI: https://doi.org/10.1016/j.jobe.2018.12.014.

14. Zhao D-X and He B-J. Effects of architectural shapes on surface wind pressure distribution: Case studies of oval-shaped tall buildings. *Journal of Building Engineering* 2017; 12: 219-228. DOI: https://doi.org/10.1016/j.jobe.2017.06.009.

15. Bady M, Kato S and Huang H. Towards the application of indoor ventilation efficiency indices to evaluate the air quality of urban areas. *Building and Environment* 2008; 43: 1991-2004. Article. DOI: 10.1016/j.buildenv.2007.11.013.

16. Hang J, Li Y and Sandberg M. Experimental and numerical studies of flows through and within high-rise building arrays and their link to ventilation strategy. *Journal of Wind Engineering and Industrial Aerodynamics* 2011; 99: 1036-1055. Article. DOI: 10.1016/j.jweia.2011.07.004.

17. Hang J, Sandberg M and Li Y. Age of air and air exchange efficiency in idealized city models. *Building and Environment* 2009; 44: 1714-1723. Article. DOI: 10.1016/j.buildenv.2008.11.013.

18. Ai ZT, Mak CM and Lee HC. Roadside air quality and implications for control

measures: A case study of Hong Kong. *Atmospheric Environment* 2016; 137: 6-16. DOI: 10.1016/j.atmosenv.2016.04.033.

19. Fang Z, Feng X, Liu J, Lin Z, Mak CM, Niu J, Tse K-T and Xu X. Investigation into the differences among several outdoor thermal comfort indices against field survey in subtropics. *Sustainable Cities and Society* 2019; 44: 676-690. DOI: https://doi.org/10.1016/j.scs.2018.10.022.

20. Ai ZT and Mak CM. Large-eddy Simulation of flow and dispersion around an isolated building: Analysis of influencing factors. *Computers & Fluids* 2015; 118: 89-100. DOI: https://doi.org/10.1016/j.compfluid.2015.06.006.

21. Du Y and Mak CM. Improving pedestrian level low wind velocity environment in high-density cities: A general framework and case study. *Sustainable Cities and Society* 2018; 42: 314-324. DOI: https://doi.org/10.1016/j.scs.2018.08.001.

22. Cheng V and Ng E. Thermal Comfort in Urban Open Spaces for Hong Kong. *Architectural Science Review* 2006; 49: 236-242. DOI: 10.3763/asre.2006.4932.

23. Ng E, Tam I, Ng A, Givoni B, Katzschner L, Kwok K and Cheng V. Feasibility study for establishment of air ventilation assessment system–final report. *Hong Kong: Department of Architecture, Chinese University of Hong Kong* 2005; 16.

24. Du Y, Mak CM and Li Y. A multi-stage optimization of pedestrian level wind environment and thermal comfort with lift-up design in ideal urban canyons.

Sustainable Cities and Society 2019; 46: 101424. DOI: https://doi.org/10.1016/j.scs.2019.101424.

25. Gao NP, Niu JL, Perino M and Heiselberg P. The airborne transmission of infection between flats in high-rise residential buildings: Tracer gas simulation. *Building and Environment* 2008; 43: 1805-1817. DOI: https://doi.org/10.1016/j.buildenv.2007.10.023.

26. Tsai MY and Chen KS. Measurements and three-dimensional modeling of air pollutant dispersion in an Urban Street Canyon. *Atmospheric Environment* 2004; 38: 5911-5924. DOI: https://doi.org/10.1016/j.atmosenv.2004.07.008.

27. Wang JS, Chan TL, Cheung CS, Leung CW and Hung WT. Three-dimensional pollutant concentration dispersion of a vehicular exhaust plume in the real atmosphere. *Atmospheric Environment* 2006; 40: 484-497. DOI: https://doi.org/10.1016/j.atmosenv.2005.09.046.

28. Jiang Y, Alexander D, Jenkins H, Arthur R and Chen Q. Natural ventilation in buildings: measurement in a wind tunnel and numerical simulation with large-eddy simulation. *Journal of Wind Engineering and Industrial Aerodynamics* 2003; 91: 331-353. DOI: https://doi.org/10.1016/S0167-6105(02)00380-X.

29. Padilla-Marcos MÁ, Meiss A and Feijó-Muñoz J. Proposal for a Simplified CFD Procedure for Obtaining Patterns of the Age of Air in Outdoor Spaces for the Natural

Ventilation of Buildings. *Energies* 2017; 10: 1252.

30. Wang X, Sun X and Yu CWF. Building envelope with variable thermal performance: Opportunities and challenges. *Indoor and Built Environment* 2018; 27: 729-733. DOI: 10.1177/1420326X18773928.

31. Dai YW, Mak CM and Ai ZT. Computational fluid dynamics simulation of wind-driven inter-unit dispersion around multi-storey buildings: Upstream building effect. *Indoor and Built Environment* 2017; 28: 217-234. DOI: 10.1177/1420326X17745943.

32. Yin H, Liu C, Zhang L, Li A and Ma Z. Measurement and evaluation of indoor air quality in naturally ventilated residential buildings. *Indoor and Built Environment* 2019; 28: 1307-1323. DOI: 10.1177/1420326X19833118.

33. Man X, Lu Y, Li G, Wang Y and Liu J. A study on the stack effect of a super high-rise residential building in a severe cold region in China. *Indoor and Built Environment* 2019; 29: 255-269. DOI: 10.1177/1420326X19856045.

34. Deng X and Tan Z. Numerical analysis of local thermal comfort in a plan office under natural ventilation. *Indoor and Built Environment* 2019; 29: 972-986. DOI: 10.1177/1420326X19866497.

35. Aflaki A, Mahyuddin N, Al-Cheikh Mahmoud Z and Baharum MR. A review on natural ventilation applications through building façade components and ventilation openings in tropical climates. *Energy and Buildings* 2015; 101: 153-162. DOI:

https://doi.org/10.1016/j.enbuild.2015.04.033.

36. Cao S-J, Yu CW and Luo X. Heating, ventilating and air conditioning system and environmental control for wellbeing. *Indoor and Built Environment* 2020; 29: 1191-1194. DOI: 10.1177/1420326X20951967.

37. Ai ZT and Mak CM. Wind-induced single-sided natural ventilation in buildings near a long street canyon: CFD evaluation of street configuration and envelope design. *Journal of Wind Engineering and Industrial Aerodynamics* 2018; 172: 96-106. DOI: https://doi.org/10.1016/j.jweia.2017.10.024.

38. Blocken B, Stathopoulos T and van Beeck JPAJ. Pedestrian-level wind conditions around buildings: Review of wind-tunnel and CFD techniques and their accuracy for wind comfort assessment. *Building and Environment* 2016; 100: 50-81. DOI: https://doi.org/10.1016/j.buildenv.2016.02.004.

39. Longo R, Fürst M, Bellemans A, Ferrarotti M, Derudi M and Parente A. CFD dispersion study based on a variable Schmidt formulation for flows around different configurations of ground-mounted buildings. *Building and Environment* 2019; 154: 336-347. DOI: https://doi.org/10.1016/j.buildenv.2019.02.041.

40. Mochida A and Lun IYF. Prediction of wind environment and thermal comfort at pedestrian level in urban area. *Journal of Wind Engineering and Industrial Aerodynamics* 2008; 96: 1498-1527. DOI:

https://doi.org/10.1016/j.jweia.2008.02.033.

41. van Druenen T, van Hooff T, Montazeri H and Blocken B. CFD evaluation of building geometry modifications to reduce pedestrian-level wind speed. *Building and Environment* 2019; 163: 106293. DOI: https://doi.org/10.1016/j.buildenv.2019.106293.

42. van Hooff T, Blocken B and Tominaga Y. On the accuracy of CFD simulations of cross-ventilation flows for a generic isolated building: Comparison of RANS, LES and experiments. *Building and Environment* 2017; 114: 148-165. DOI: https://doi.org/10.1016/j.buildenv.2016.12.019.

43. Yoshie R, Mochida A, Tominaga Y, Kataoka H, Harimoto K, Nozu T and Shirasawa T. Cooperative project for CFD prediction of pedestrian wind environment in the Architectural Institute of Japan. *Journal of Wind Engineering and Industrial Aerodynamics* 2007; 95: 1551-1578. DOI: https://doi.org/10.1016/j.jweia.2007.02.023.

44. Leitl B and Schatzmann M. Compilation of experimental data for validation purposes. Hamburg: Meteorology Institute, Hamburg University, 1998.

45. An K, Fung JCH and Yim SHL. Sensitivity of inflow boundary conditions on downstream wind and turbulence profiles through building obstacles using a CFD approach. *Journal of Wind Engineering and Industrial Aerodynamics* 2013; 115: 137-

149. DOI: https://doi.org/10.1016/j.jweia.2013.01.004.

46. Xia Q, Niu J and Liu X. Dispersion of air pollutants around buildings: A review of past studies and their methodologies. London, England2014, p. 201-224.

47. Blocken B. Computational Fluid Dynamics for urban physics: Importance, scales, possibilities, limitations and ten tips and tricks towards accurate and reliable simulations. *Building and Environment* 2015; 91: 219-245. DOI: https://doi.org/10.1016/j.buildenv.2015.02.015.

48. Liu J and Niu J. CFD simulation of the wind environment around an isolated high-rise building: An evaluation of SRANS, LES and DES models. *Building and Environment* 2016; 96: 91-106. DOI: 10.1016/j.buildenv.2015.11.007.

49. Lateb M, Masson C, Stathopoulos T and Bedard C. Comparison of various types of k- epsilon models for pollutant emissions around a two-building configuration. *Journal of Wind Engineering and Industrial Aerodynamics* 2013; 115: 9-21. DOI: 10.1016/j.jweia.2013.01.001.

50. Tominaga Y and Stathopoulos T. Numerical simulation of dispersion around an isolated cubic building: Comparison of various types of k–ε models. *Atmospheric Environment* 2009; 43: 3200-3210. DOI: https://doi.org/10.1016/j.atmosenv.2009.03.038.

51. Tien PW and Calautit JK. Numerical analysis of the wind and thermal comfort in

courtyards “skycourts” in high rise buildings. *Journal of Building Engineering* 2019; 24: 100735. DOI: https://doi.org/10.1016/j.jobe.2019.100735.

52. Ai ZT and Mak CM. A study of interunit dispersion around multistory buildings with single-sided ventilation under different wind directions. *Atmospheric Environment* 2014; 88: 1-13. DOI: https://doi.org/10.1016/j.atmosenv.2014.01.049.

53. ANSYS FLUENT 14.5. Canonsburg, PA, USA: ANSYS, Inc., 2012.

54. Ai ZT and Mak CM. CFD simulation of flow and dispersion around an isolated building: Effect of inhomogeneous ABL and near-wall treatment. *Atmospheric Environment* 2013; 77: 568-578. DOI: https://doi.org/10.1016/j.atmosenv.2013.05.034.

55. Richards PJ and Hoxey RP. Appropriate boundary conditions for computational wind engineering models using the k-ϵ turbulence model. *Journal of Wind Engineering and Industrial Aerodynamics* 1993; 46-47: 145-153. DOI: https://doi.org/10.1016/0167-6105(93)90124-7.

56. Gorlé C, van Beeck J and Rambaud P. Dispersion in the Wake of a Rectangular Building: Validation of Two Reynolds-Averaged Navier–Stokes Modelling Approaches. *Boundary-Layer Meteorology* 2010; 137: 115-133. journal article. DOI: 10.1007/s10546-010-9521-0.

57. Liu J, Zhang X, Niu J and Tse KT. Pedestrian-level wind and gust around

buildings with a ‘lift-up’ design: Assessment of influence from surrounding buildings by adopting LES. *Building Simulation* 2019; 12: 1107-1118. DOI: 10.1007/s12273-019-0541-5.

58. Yu H and Thé J. Simulation of gaseous pollutant dispersion around an isolated building using the k–ω SST (shear stress transport) turbulence model. *Journal of the Air & Waste Management Association* 2017; 67: 517-536. DOI: 10.1080/10962247.2016.1232667.

59. Blocken B, Stathopoulos T and Carmeliet J. CFD simulation of the atmospheric boundary layer: wall function problems. *Atmospheric Environment* 2007; 41: 238-252. DOI: https://doi.org/10.1016/j.atmosenv.2006.08.019.

60. Franke J, Hellsten A, Schlünzen H and B. Carissimo. *Cost Action 732: Best Practice Guideline for the CFD Simulation of Flow in the Urban Environment, in: Quality Assurance and Impovement of Microscale Meteorological Models,*. Brussels: Meteorological Inst., 2007.

61. Tominaga Y, Mochida A, Yoshie R, Kataoka H, Nozu T, Yoshikawa M and Shirasawa T. AIJ guidelines for practical applications of CFD to pedestrian wind environment around buildings. *Journal of Wind Engineering and Industrial Aerodynamics* 2008; 96: 1749-1761. DOI: https://doi.org/10.1016/j.jweia.2008.02.058.

62. Montazeri H and Blocken B. CFD simulation of wind-induced pressure coefficients on buildings with and without balconies: Validation and sensitivity analysis. *Building and Environment* 2013; 60: 137-149. DOI: https://doi.org/10.1016/j.buildenv.2012.11.012.